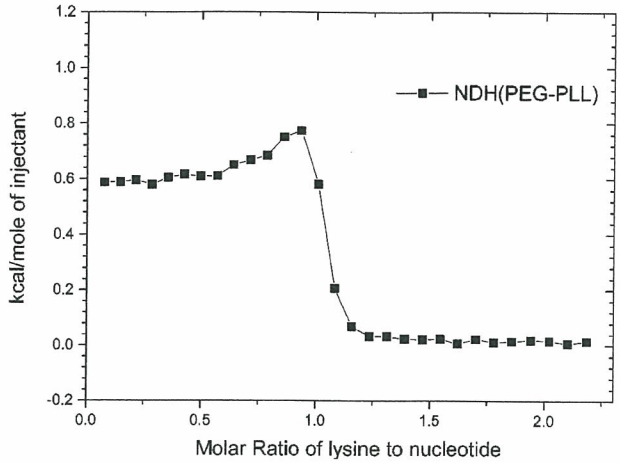

Figure 3. Integrated ITC curve of PEG−PLL binding to plasmid pGL3 DNA in water with 10 mM NaCl. The endothermic binding was completed by the charge ratio of 1.2.

was entropically driven. This result is in good agreement with those reported by other researchers.[2,4]

In this system, the initial binding stage was completed with the charge ratio of 0.9. The second stage was observed when a further addition of cobalt hexamine occurred. No heat was generated at the region in the charge ratio range higher than 1.5. From the results of turbidity measurement, a significant decrease in the transmittance resulting from the formation of aggregates was observed immediately following the second binding stage (data not shown). After the titration measurement, precipitates were visually observed in the sample solution.

The integrated ITC curve of the PEG−PLL binding to pDNA is shown in Figure 3, indicating an endothermic ligand binding the same as that observed in the $Co(NH_3)_6^{3+}$/pDNA system. Although the two-stage binding observed in the ITC curve of the cobalt hexamine titration is well separated, no segregation was observed in the ITC profile for the PEG−PLL/pDNA system. The PEG−PLL binding was completed with the charge ratio of 1.2.

Development of the Novel Fitting Model

A novel fitting model is based on the combination of the single set of identical sites (SSIS) model. Let us introduce the SSIS model as follows.[11,12] Generally, the binding constant K and the relationship of the total and free ligand concentrations (X_t and $[X]$) are represented by eqs 1 and 2, respectively

$$K = \frac{\Theta}{(1-\Theta)[X]} \quad (1)$$

$$X_t = [X] + N\Theta M_t \quad (2)$$

where N is the number of binding sites, M_t is the total concentration of macromolecule, and Θ is the fractional sites occupied by ligand. Combining eqs 1 and 2 gives eq 3

$$\Theta^2 - \Theta\left[1 + \frac{X_t}{NM_t} + \frac{1}{NKM_t}\right] + \frac{X_t}{NM_t} = 0 \quad (3)$$

The total heat content Q of the solution contained in the sample cell at fractional saturation Θ is

$$Q = N\Theta M_t \Delta H V_o \quad (4)$$

where ΔH is the molar heat of ligand binding and V_o is the cell

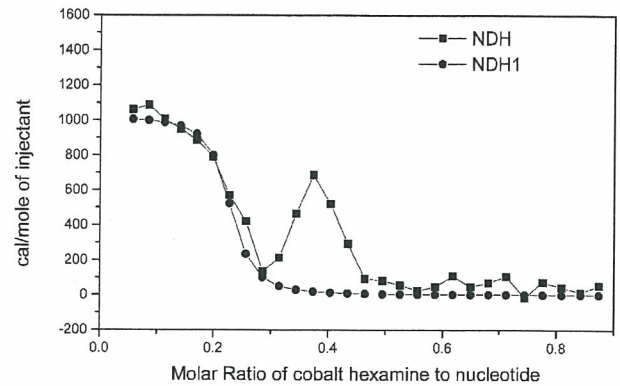

Figure 4. Integrated ITC curve of cobalt hexamine binding to plasmid pGL3 DNA (■) and representative ITC curve NDH1 generated from the SSIS model with the following fitting parameter (●). $N_1 = 0.216 \pm 0.004$, $K_1 = (17.79 \pm 4.99) \times 10^5\ M^{-1}$, $\Delta H_1 = 1019 \pm 30$ cal/mol.

volume. Solving the quadratic eq 3 for Θ and then substituting this into eq 4 gives eq 5

$$Q = \frac{NM_t\Delta HV_o}{2}[1 + (X_t/NM_t) + (1/NKM_t) - \sqrt{(1 + (X_t/NM_t) + (1/NKM_t))^2 - (4X_t/NM_t)}] \quad (5)$$

The value of Q can be calculated for any designated values of N, K, and ΔH at the end of the ith injection and designated $Q(i)$. The parameter of interest for comparison with the experiment, however, is the change in heat content from the completion of the $(i-1)$th injection to completion of the i-th injection. The expression for Q in eq 5 only applies to the liquid contained in volume V_o. Therefore, after an injection is completed, it is obvious that a correction must be made for the displaced volume (i.e., ΔV_i = injection volume) since some of the liquid in V_o after the $(i-1)$th injection will no longer be in V_o after the ith injection, even though it will contribute to the heat effect (assuming that the kinetics of the reaction and mixing are fast) before it passes out of the working volume V_o. The liquid in the displaced volume contributes about 50% as much heat effect as an equivalent volume remaining in V_o. The correct expression for the heat released $\Delta Q(i)$ from the ith injection is

$$\Delta Q(i) = Q(i) + \frac{dV_i}{V_o}\left[\frac{Q(i) + Q(i-1)}{2}\right] - Q(i-1) \quad (6)$$

By dividing $\Delta Q(i)$ with moles in the ith injected volume, the normalized heat, NDH(i), is obtained. Hereafter, NDH(i) is described by NDH(N, ΔH, K) because NDH(i) is dependent on the three parameters, N, ΔH and K.

A set of fitting parameters, N_1, K_1, and ΔH_1, is assigned to the initial binding stage of cationic ligands to the elongated pDNA, and another set, N_2, K_2, and ΔH_2, is assigned to the second binding stage during the pDNA conformational transition. On the basis of the SSIS model, the optimum fitting parameters for the initial stage provide the most suitable ITC curve as shown in Figure 4.

On comparison of the ITC curves for the PEG−PLL/pDNA system with that for $Co(NH_3)_6^{3+}$/pDNA, the molar ratios where the second binding stage appeared disagree. It is assumed that the second binding stage in the PEG−PLL system is immediately generated after the initial binding stage. In the system of cobalt hexamine, however, the generation of the second stage requires an excess amount of ligand in the bulk solution, corresponding to the delay of the second stage in Figure 2. As

shown in Figure 3, the second stage in the PEG−PLL system was almost finished around the charge equivalent condition. Therefore, both the initial and second binding stages in the PEG−PLL system coexist in a certain region where the molar ratio is greater than 0.5. This binding feature agrees with the results obtained from the direct observation of the DNA condensation using fluorescence microscopy.[21]

On the contrary, the two binding stages were well separated in the system of cobalt hexamine. In this system, the second binding stage during the DNA conformational change occurs after the initial stage where the fraction of the bound ligand reaches the critical one and all of the injected cationic ligands are consumed in the initial binding stage. As the injections of the cationic ligands are repeated, the amount of bound ligands gradually increases and reaches a maximum value at the molar ratio of 0.3, corresponding to the critical residual charges of the elongated DNA double helices, i.e., the end point of the initial binding stage. Under this condition, the added ligands do not tend to bind the elongated DNA, then the heat generated by the binding gradually decreases. The further addition of cationic ligands induces the DNA conformational change or "DNA condensation". During this transition, the second binding stage of the cationic ligands is promoted. The presence or absence of the delay between the two binding stages seems to be a significant phenomenological difference. Therefore, the effect of this delay is taken into consideration in the novel fitting model developed in this study.

Prior to describing the delay of the second binding stage observed in the $Co(NH_3)_6^{3+}$/pDNA system, the curve fitting for the second binding stage should be discussed here. On the basis of the SSIS model, a general ITC curve should be produced as a decreased sigmoidal curve as shown in Figure 4 (NDH1). According to the results of the DNA conformational analysis under fluorescence microscopy, both the elongated and collapsed DNA chains coexist during the transition region of the DNA condensation.[22] Thus, the population of collapsed DNAs should gradually increase with an increase in the molar ratio. This leads to the decrease in the fraction of ligands bound to the elongated DNA and the increase in that of the collapsed one. If the delay in the second binding stage was missing, the residual ligands not involved in the initial binding stage ideally contribute to the second binding stage. The amount of this residual ligand is represented by differences between the maximum and each fraction of the binding ligand, which can be expressed by an increased sigmoidal curve. Because the sigmoidal NDH having N, K, ΔH as a variable is linearly dependent on the fraction of ligands (Θ), Θ can be described as the absolute value of NDH divided by ΔH, ABS(NDH/ΔH).

To describe the fraction of the occupied site on DNA during the second binding stage, an NDH3 sigmoidal curve was employed. The definition of parameters for NDH3 is basically the same as those for the NDH1, but only N_3 is variable when considering the delay of the second binding stage. When N_3 is equal to N_1, the initial binding stage is immediately followed by the second binding stage during the DNA condensation. On the contrary, as N_3 becomes larger than N_1, the second binding stage is separated from the initial binding stage, indicating that the delay in the second stage is significant in the ITC curve. Thus, the fraction of the occupied site on DNA during the second stage is represented by ABS((ΔH_1 − NDH3)/ΔH_1) in Figure 5, which is derived from 1 − ABS(NDH3/ΔH_1). We intend to generate for the second binding stage the NDH2 curve which is a function of N_2, K_2, and ΔH_2. The second binding stage of the ITC curve was fitted by the product of the

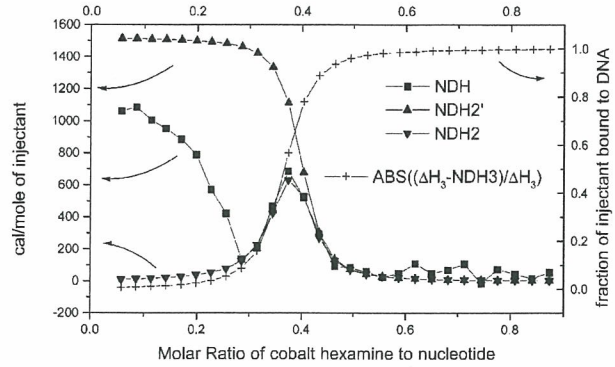

Figure 5. Representative curve for the second binding stage during pDNA condensation (NDH2; ▼).

hypothetical ITC curve NDH2′ and the increased sigmoidal curve ABS((ΔH_1 − NDH3)/ΔH_1). The ITC curve NDH2′ that corresponds to a standard ITC curve with the absence of the initial binding stage is generated by the SSIS model, indicating that the NDH2′ curve is defined by N_2', K_2', and $\Delta H_2'$. The product was defined as NDH2 where $N_2' - N_3$ (the difference of N_2' and N_3), K_2', and $\Delta H_2'$ are selected for N_2, K_2, and ΔH_2, respectively.

Application of New Model

The optimum fittings for the experimental ITC curves of both $Co(NH_3)_6^{3+}$/pDNA and PEG−PLL/pDNA are shown in Figures 6 and 7, respectively. The ITC curves were fitted by the sum of NDH1 and NDH2, corresponding to the initial and second binding stages, respectively. The sum of these two curves represents the relation of the total heats accompanied by ligand binding on DNA to the mixing ratio. Although the curve NDH1 is defined by the set of three parameters, N_1, K_1, and ΔH_1, another curve, NDH2, was defined by the set of six parameters, N_3, K_1, ΔH_1, N_2', K_2', and $\Delta H_2'$. In this method, both curves, NDH1 and NDH2, were simultaneously fitted. The difference in N_2' and N_3, which is described by N_2, means the binding stoichiometry for the second binding stage in the novel fitting model, and the difference in N_1 and N_3 reflects the delay of the second binding stage. The important thermodynamic parameters are listed in Tables 1 and 2. For both the simplified notation and comparison with the reported data, the binding stoichiometry for the second binding stage is represented by the parameter N_2 in the tables.

Discussion

The cooperative binding of polycations to DNA chains has been discussed as a typical binding feature of polyelectrolytes. Similar binding processes have already been independently considered by McGhee and von Hippel[23] and by Schwarz.[24] MaGhee and von Hippel suggested the concept of cooperativity of protein binding to DNA using the following three binding modes: (1) the binding to the isolated site with an intrinsic binding constant K, (2) a singly contiguous site to which a linear polymer binds with binding constant $K\omega$, and (3) a doubly contiguous site to which a linear polymer binds with binding constant $K\omega^2$, where ω is the cooperativity constant. When $\omega > 1$, the cationic ligands attract each other and the binding is positively cooperative; when $\omega < 1$, the cationic ligands repel each other and the binding is anti or negatively cooperative; when $\omega = 1$, neither cooperativity is observed during the binding.

Schwarz's theory also implies two types of intrinsic binding processes: (1) the binding of isolated ligands with binding

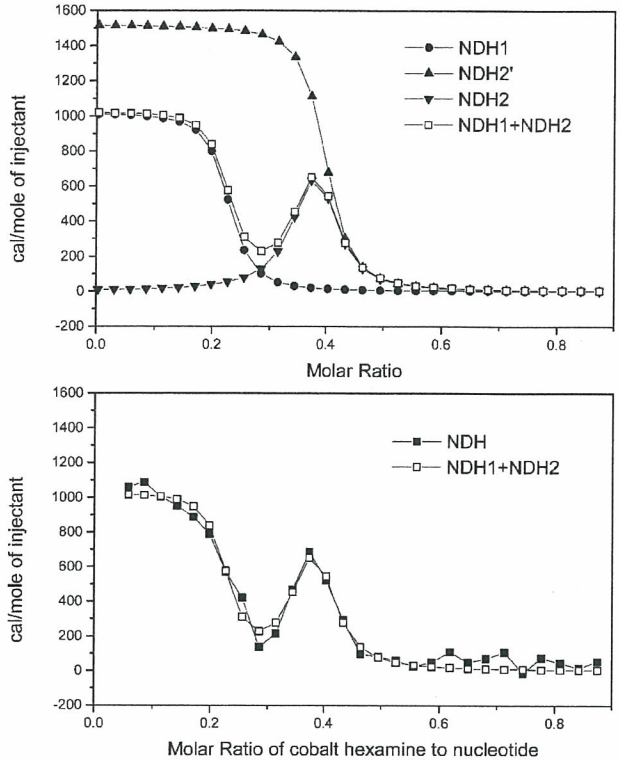

Figure 6. Optimum fitting for the experimental ITC curve (■) of $Co(NH_3)_6^{3+}$/pDNA, NDH1 + NDH2 (□). NDH1 (●) represents the initial binding stage corresponding to that in Figure 4. NDH2′ (▲) and NDH2 (▼) are the same as those in Figure 5. NDH1 + NDH2 is used for the fitting of the experimental ITC curve; $N_1 = 0.216 \pm 0.004$, $K_1 = (17.79 \pm 4.99) \times 10^5\ M^{-1}$, $\Delta H_1 = 1019 \pm 30$ cal/mol, $N_2' = 0.385 \pm 0.012$, $N_3 = 0.354$, $N_2 = N_2' - N_3 = 0.031 \pm 0.012$, $K_2 = K_2' = (27.82 \pm 12.61) \times 10^5\ M^{-1}$, $\Delta H_2 = \Delta H_2' = 1520 \pm 301$ cal/mol.

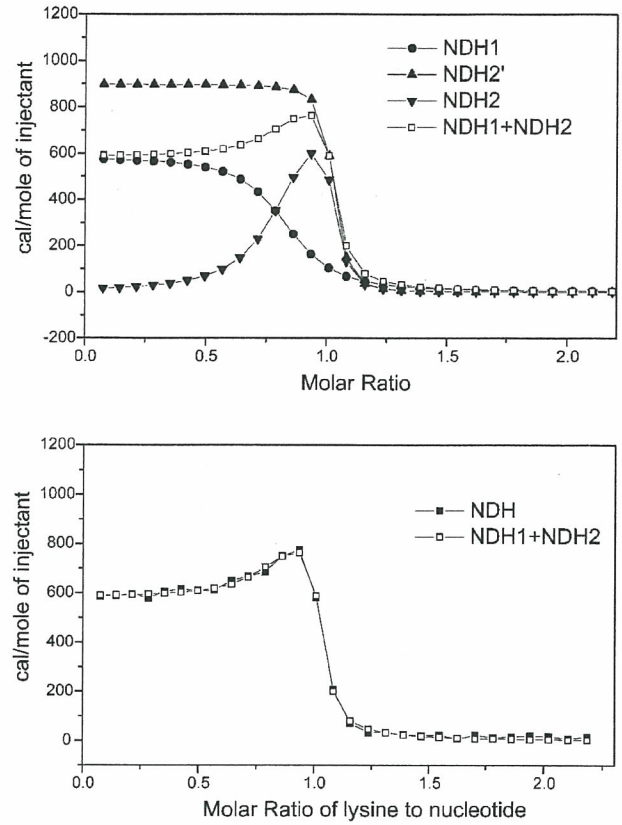

Figure 7. Optimum fitting for the experimental ITC curve (■) of PEG−PLL/pDNA, NDH1 + NDH2 (□). NDH1 (●) represents the initial binding stage corresponding to those of the PEG−PLL/pDNA system shown in Figures 5 and 6. NDH2′ (▲) and NDH2 (▼) correspond to those in Figure 6. NDH1 + NDH2 is used for the fitting of the experimental ITC curve: $N_3 = N_1 = 0.810 \pm 0.026$, $K_1 = (2.66 \pm 0.62) \times 10^5\ M^{-1}$, $\Delta H_1 = 585 \pm 5$ cal/mol, $N_2' = 0.994 \pm 0.005$, $N_2 = N_2' - N_3 = 0.184 \pm 0.031$, $K_2 = K_2' = (51.07 \pm 13.98) \times 10^5\ M^{-1}$, $\Delta H_2 = \Delta H_2' = 899 \pm 37$ cal/mol.

constant K (nucleation), and (2) the binding of ligands to the nearest-neighbor binding site (aggregation) with binding constant Kq, where q is the cooperativity parameter. In both models, the binding process with the binding constant $K\omega$ or Kq is generated by the initial ligand binding with binding constant K, which is the matter of our concern. Let us assume that K_2 was equal to $K\omega$ or Kq. For the cobalt hexamine binding to DNA, ω or q is estimated to be 1.56, which is obtained by K_2/K_1 using the parameters shown in Table 1. For the PEG−PLL binding to DNA, ω or q is estimated to be 19.20 using the parameters shown in Table 2. In both cases, it is obvious that the binding constant K_2 seems to be significantly enhanced and the estimation for the cobalt hexamine binding is inconsistent with the reported data.[2] Although the above classification was suggested to explain the cooperative binding of the cationic ligands, it is not clear in this study whether such kinds of cooperativities induced by the ligand−ligand interactions exist in the binding of the cobalt hexamine or PEG−PLL to pDNA.

In this study, it was assumed that the positive cooperative binding of the cobalt hexamine or PEG−PLL to DNA is attributed to the conformational change in DNA rather than the interaction between the same chemicals. The DNA conformational change produces the environmental modulation around the DNA vicinity, and this may affect the binding features of the cationic ligands. Hud et al. suggested that the effect of the DNA segment fluctuation induces the enhanced binding of cationic ligands to a loop formed by two sequence-separated sections in close contact.[25] The cationic ligands bind to this contact and stabilize the loop. Successive ligands bind both the loop and extended DNA to induce the collapsed form. Therefore, the binding constants K_1 and K_2 are treated as individual variables in this study.

To develop a flexible fitting method, different types of ligands, a low-molecular weight metal complex cobalt hexamine and block copolymer PEG−PLL, were employed in this study. Cobalt hexamine is a widely used chemical as a standard reagent of DNA condensation. On the contrary, PEG−PLL is a relatively recently developed reagent as a gene carrier.[19] As exemplified by the presence or absence of the delay in the appearance of the second binding stage in Figures 2 and 3, the condensation mechanism seems to be slightly different from each other despite the same driving force, the electrostatic interaction. It was reported that this difference becomes enhanced in the dilute DNA solution experiments and the latter more effectively induces the DNA condensation.[21]

Under such situations, the charge equivalent mixing ratio between PEG−PLL and DNA is enough to induce the DNA condensation, while an excess amount of cobalt hexamine, at least several times that of the phosphate residue, should be required. A similar trend was observed in the ITC curves obtained in this study. The charge ratio at the end point of the PEG−PLL titration was 1.2, while that of cobalt hexamine was slightly higher than this value. This difference was mainly caused by their chemical structures. In this study, a simple comparison of the thermodynamic parameters N_1 and K_1 in the

TABLE 1: Parameters Obtained by Various Fitting Methods

	N_1	$K_1/10^5$ (M^{-1})	ΔH_1 (cal/mol)	N_2	$K_2/10^5$ (M^{-1})	ΔH_2 (cal/mol)
this work[a]	0.216 ± 0.004	17.79 ± 4.99	1019 ± 30	0.031 ± 0.012	27.82 ± 12.61	1520 ± 301
ref 2[b]	0.217 ± 0.012	2.30 ± 0.80	1240 ± 100	0.059 ± 0.012	6.00 ± 1.60	820 ± 90
origin[c]	0.218 ± 0.010	74.02 ± 142.4	1086 ± 68	not converged		

[a] This work: developed by this work. [b] ref 2: reported in reference 2. [c] Origin: by applying the two sets of independent sites (TSIS) model to each binding process divided from the experimental ITC curve shown in Figure 2, which is the same method as that used in the ref 2. $N_2' = 0.385 \pm 0.012$, $N_3 = 0.354$, N_2 ($=N_2' - N_3$) $= 0.031 \pm 0.012$, $K_2 = K_2'$, $\Delta H_2 = \Delta H_2'$.

TABLE 2: Parameters Obtained by Various Fitting Methods

	N_1	$K_1/10^5$ (M^{-1})	ΔH_1 (cal/mol)	N_2	$K_2/10^5$ (M^{-1})	ΔH_2 (cal/mol)
this work[a]	0.810 ± 0.026	2.66 ± 0.62	585 ± 5	0.184 ± 0.031	51.07 ± 13.98	899 ± 37
origin[b]	0.781 ± 0.032	139.10 ± 44.19	584 ± 9	0.222 ± 0.034	7.2 ± 2.23	973 ± 77

[a] This work: developed by this work. [b] Origin: by applying TSIS model to the ITC curve shown in Figure 3. $N_3 = N_1$, $N_2' = 0.994 \pm 0.005$, N_2 ($=N_2' - N_3$) $= 0.184 + 0.031$, $K_2 = K_2'$, $\Delta H_2 = \Delta H_2'$.

cobalt hexamine system with those of PEG−PLL makes no realistic sense, because the former was analyzed in a molar unit and the latter was summarized in a charge unit. On comparison of N_1 with the consideration of the valency, however, it is obvious that PEG−PLL more effectively binds (see Tables 1 and 2).

In the novel fitting model developed in this study, the cationic ligand binding to DNA was classified into two stages, the initial and second binding stages. The former has the binding constant K_1 and the latter K_2. Regarding the magnitude relationship of the binding constants, Teif and Lando theoretically pointed out that the DNA conformational change to the collapsed state takes place when $K_2 > K_1$.[16] In the general curve fitting models for the experimental ITC curves, however, this assumption could not be taken into consideration. Although general fitting models that can treat multiple binding sites have the assumption $K_1 > K_2$, our model is not restricted by this assumption. To treat two binding stages as individual events, they were characterized in relation to the conformational change in pDNA. Thus, the former occurs when the DNA conformation retained as the elongated state and the latter is promoted during the DNA conformational change.

Generally, there is a significant difficulty in the separation of the two binding stages, when the overlap of the initial and second binding stages was observed as shown in the PEG−PLL system. Despite the absence of the saddle point in the integrated ITC curve for the PEG−PLL system, the assumption of two-stage binding is plausible, because the discrete transition between the elongated and collapsed states was essentially the same as that observed in the cobalt hexamine system.[21] Table 1 shows a comparison of the thermodynamic parameters determined in this study with those by other methods reported in ref 2 and obtained by the manufacturer recommended method that is based on the two sets of independent sites (TSIS) model. Although the second set of parameters did not converge using the TSIS model, no significant difference was observed in both values of N_1 and N_2. As mentioned in the Introduction, the TSIS model should not be applied to the particular system where K_1 is smaller than K_2, because this model is constructed assuming that K_1 is greater than K_2. This is the reason the second set of parameters was not determined by the TSIS model.

Matulis et al. also employed the TSIS model, but they completely divided the integrated ITC curve by the saddle point. In their method, two parts of the ITC curve were separately fitted.[2] Therefore, the magnitude relationship of K_1 and K_2 would not be discussed under their framework. On the contrary, both parts were simultaneously fitted in this study. In addition, when their method was applied to the PEG−PLL system, the curve fitting was done under the restricted assumption $K_1 > K_2$. However, our method is not restricted by this assumption. Among these three methods, thus, an appropriate method suitable for the discussion on the magnitude relationship of K_1 and K_2 is considered to be limited to the novel method developed in this study.

The charge ratio of the cationic ligands to DNA is expressed by the total stoichiometry, the sum of N_1 and N_2. On the basis of the consideration of the valence of cobalt hexamine, the charge ratio is estimated to be 0.72 in this study, suggesting that the residual ligands do not directly contribute to the DNA condensation (see Table 1). This trend is consistent with another report.[2] It is still controversial that the results of the ITC experiments disagree with the theoretical prediction of the two-variable counterion condensation theory.[14] As for the PEG−PLL system, the charge ratio was determined to be 0.99, indicating that almost all of the negative charge of the DNA phosphate is neutralized by the ligand binding (see Table 2). The result of the charge equivalent complexation agrees with those obtained from the single molecule observation under fluorescence microscopy.[20] This difference in the binding stoichiometry between cobalt hexamine and PEG−PLL reflects the strength of the electrostatic interaction between the cationic ligands and DNA phosphates.

Conclusion

The novel fitting method based on the SSIS model for the experimental ITC curve was developed and applied to the cationic ligands binding to DNA, cobalt hexamine, and PEG−PLL systems in this study. It is demonstrated that this curve fitting method can be applicable for both systems. As for the cobalt hexamine system, the thermodynamic parameters obtained by the novel fitting method have a similar trend with those reported by other researchers. It was suggested that this method is applicable for the PEG−PLL system, in which the separation of the two binding events is not enough for the appearance of the experimental ITC curve. Although other fitting methods are applicable under the restricted assumption $K_1 > K_2$, our method, unrestricted by this assumption, is widely applicable for both cases, $K_1 > K_2$ and $K_2 > K_1$.

Acknowledgment. We thank Mr. S. Fukushima of Nippon Kayaku Co., Ltd., Japan, for the kind donation of the PEG−PLL block copolymer. This work was partially supported by a grant-in-aid for scientific research from the Ministry of Education, Culture, Sports, Science, and Technology of Japan (MEXT), the Core Research Program for Evolutional Science and Technology (CREST) from the Japan Science and Technol-

ogy Agency (JST), and 21st century COE program "Human-Friendly Materials based on Chemistry" from MEXT.

References and Notes

(1) Spink, C. H.; Chaires, J. B. *J. Am. Chem. Soc.* **1997**, *119*, 10920−10928.

(2) Matulis, D.; Rouzina, I.; Bloomfield, V. A. *J. Mol. Biol.* **2000**, *296*, 1053−1063.

(3) Bronich, T.; Kabanov, A. V.; Marky, L. A. *J. Phys. Chem. B* **2001**, *105*, 6042−6050.

(4) Matulis, D.; Rouzina, I.; Bloomfield, V. A. *J. Am. Chem. Soc.* **2002**, *124*, 7331−7342.

(5) Pozharski, E.; MacDonald, R. C. *Biophys. J.* **2002**, *83*, 556−565.

(6) Keller, M.; Tagawa, T.; Preuss, M.; Miller, A. D. *Biochemistry* **2002**, *41*, 652−659.

(7) Keller M.; Jorgensen, M. R.; Perouzel, E.; Miller, A. D. *Biochemistry* **2003**, *42*, 6067−6077.

(8) Ehtezazi, T.; Rungsardthong, U.; Stolnik, S. *Langmuir* **2003**, *19*, 9387−9394.

(9) Rungsardthong, U.; Ehtezazi, T.; Bailey, L.; Armes, S. P.; Garnett, M. C.; Stolnik, S. *Biomacromolecules* **2003**, *4*, 683−690.

(10) Nisha, C. K.; Manorama, S. V. *Langmuir* **2004**, *20*, 2386-2396.

(11) Freire, E.; Mayorga, O. L.; Straume, M. *Anal. Chem.* **1990**, *62*, 950A-959A.

(12) ITC Data Analysis in Origin, Ver.5.0; MicroCal, Inc.: Studio City, CA, 1998; pp 73−78.

(13) (a) Oosawa, F. *Polyelectrolytes*; Marcel Dekker: New York, 1971. (b) Manning, G. S. *Q. Rev. Biophys.* **1978**, *11*, 179−246.

(14) Wilson, R. W.; Bloomfield, V. A. *Biochemistry* **1979**, *18*, 2192−2196.

(15) Yamasaki, Y.; Teramoto, Y.; Yoshikawa, K. *Biophys. J.* **2001**, *80*, 2823−2832.

(16) Teif, V. B.; Lando, D. Y. *Mol. Biol.* **2001**, *35*, 106−107.

(17) Mel'nikov, S. M.; Sergeyev, V. G.; Yoshikawa, K. *J. Am. Chem. Soc.* **1995**, *117*, 9951−9956.

(18) Bloomfield,V. A. *Curr. Opin. Struct. Biol.* **1996**, *6*, 334−341.

(19) Katayose, S.; Kataoka, K. *Bioconjugate Chem.* **1997**, *8*, 702−707.

(20) Harada A.; Kataoka K. *Macromolecules* **1995**, *28*, 5294−5299.

(21) Yamasaki, Y.; Katayose, S.; Kataoka, K.; Yoshikawa, K. *Macromolecules* **2003**, *36*, 6276−6279.

(22) Yoshikawa, K.; Kidoaki, S.; Takahashi, M.; Vasilevskaya, V. V.; Khokhlov, A. R. *Ber. Bunsen-Ges. Phys. Chem.* **1996**, *100*, 876−880.

(23) McGhee, J. D.; von Hippel, P. H. *J. Mol. Biol.* **1974**, *86*, 469−489.

(24) Schwarz, G. *Eur. J. Biochem.* **1970**, *12*, 442−453.

(25) Hud, N. V.; Downing, K. H.; Balhorn, R. *Proc. Natl. Acad. Sci. U.S.A.* **1995**, *92*, 3581−3585.

Knee Surg Sports Traumatol Arthrosc (2006) 14:1094–1100
DOI 10.1007/s00167-006-0129-3

KNEE

Long term results of anterior cruciate ligament reconstruction with iliotibial tract: 6-, 13-, and 24-year longitudinal follow-up

Satoshi Yamaguchi · Takahisa Sasho · Akihiro Tsuchiya · Yuichi Wada · Hideshige Moriya

Received: 16 November 2005 / Accepted: 13 February 2006 / Published online: 15 July 2006

Abstract Many studies have reported successful outcomes less than 10 years after anterior cruciate ligament (ACL) reconstruction. However, longer-term outcomes have not been analyzed. We assessd outcomes 24 years after anterior cruciate ligament reconstruction with iliotibial tract and compared them with shorter-term results in the same patients. Between 1979 and 1981, 45 patients underwent combined intra- and extra-articular ACL reconstruction with iliotibial tract. Follow-up evaluations of these patients were performed at 6, 13, and 24 years after surgery, which included manual and instrumental laxity testing, functional assessments, and radiography. Twenty-six (60%) patients of the original ACL reconstruction cohort participated in all three follow-up assessments. Three patients had undergone meniscectomy prior to ACL reconstruction and 18 underwent meniscectomy together with ACL reconstruction. Eleven patients underwent subsequent meniscectomy. The mean Lysholm score was 96.2, 93.8, and 87.8 at 6-, 13-, and 24-year follow-up, respectively. A significant decrease in mean Lysholm score was found between 13- and 24-year follow-up. The mean KT-1000 side-to-side difference was 3.5 mm at 24-year follow-up. Overall knee laxity did not change significantly during the follow-up period. At 24-year follow-up, 17 (71%) patients had moderate or severe degenerative changes on radiographs although about 50% of the patients participated in regular sports activities and no patient required regular clinical intervention.

Keywords ACL · Reconstruction · Long-term results · Iliotibial tract · Degenerative change

S. Yamaguchi · T. Sasho (✉) · H. Moriya
Department of Orthopaedic Surgery,
Graduate School of Medicine, Chiba University,
1-8-1 Inohana, Chuo-ku, Chiba 260-8677, Japan
e-mail: sasho@faculty.chiba-u.jp

A. Tsuchiya
Funabashi Orthopaedic Sports Medicine Center,
1-833 Hazama, Funabashi, Chiba 274-0822, Japan

Y. Wada
Department of Orthopaedic Surgery, Ichihara Hospital,
Teikyo University School of Medicine, 3426-3 Anesaki,
Ichihara, Chiba 299-0111, Japan

Introduction

Rupture of the anterior cruciate ligament (ACL) is one of the most common injuries in sports activities and more than 100,000 ACL injuries occur each year in young athletes in the United States [11]. In many cases, surgical reconstruction of the ligament is recommended, with the primary goal of surgery being restoration of knee stability. Many studies have reported successful short-term and intermediate-term results following ACL reconstruction [8, 14, 17, 31, 34]; however, longer-term outcomes have not been well studied. To our knowledge, only six studies have analyzed outcomes more than 10 years after surgery [6, 13, 18, 20, 25, 26]. Even longer follow-up periods should be evaluated, since most patients who undergo ACL reconstruction are young and remain active in sports for 15 or more years after surgery [2]. In addition, Shelbourne et al. [30] suggested that long-term follow-up should be performed consistently at 10, 15, and 20 years after ACL reconstruction because damage to

the knee joint does not appear to be affecting knee function until approximately 7 years after surgery.

In our hospital, ACL reconstruction with iliotibial tract (ITT) has been performed since 1979. The purpose of this study was to evaluate 24-year results after this technique and to compare them with those of 6- and 13-year follow-ups in the same patient cohort.

Materials and methods

Patients

Between 1979 and 1981, a total of 45 patients (32 males, 13 females) underwent ACL reconstruction in our hospital and an affiliated hospital. The mean age at surgery was 23.9 years (range 15–43 years). The mean interval from injury to surgery was 33.3 months (range 1–218 months). The follow-up, which consisted of physical examination and objective testing, was conducted three times at 6, 13 and 24 years after surgery. The present study includes only patients who completed all three follow-up visits.

Surgical technique

The surgical procedure consisted of intra- and extra-articular reconstruction with ITT. All surgeries were performed by two experienced orthopedic surgeons, including one senior author (HM).

A 25-cm longitudinal incision that dissected the subcutaneous tissue, was made on the lateral aspect of the thigh. A 2.5-cm-wide distally, 4-cm-wide proximally, and 22-cm-long strip of the ITT graft was harvested, leaving the tibial insertion (Gerdy's tubercle) attached. A 7.5-mm femoral hole was then drilled in an outside-in fashion. The entry point was 1 cm superior and 1 cm posterior to the origin of the fibular collateral ligament, and the intra-articular outlet was the superomedial corner of the lateral femoral condyle, just anterior to the joint capsule. A separate medial parapatellar incision was made. Thorough intra-articular pathology was investigated and meniscectomy was performed if necessary. A 7.5-mm tibial tunnel was drilled under direct vision from medial to the tibial tuberosity to the anterior half of the ACL stump. With forceps, the graft was passed deep to the fibular collateral ligament and through the femoral and tibial tunnels. With the knee at 90° flexion and the foot externally rotated, the graft was pulled taut and sutured to the fibular collateral ligament and the periosteum of the lateral femoral condyle. Then, with the knee at 30°flexion and the foot kept externally rotated, the graft was sutured to the periosteum around the outlet of the tibial tunnel (Fig. 1).

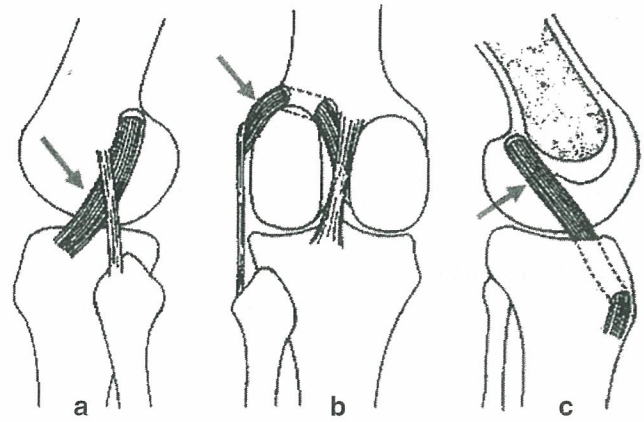

Fig. 1 Lateral (**a**), posterior (**b**), and intercondylar (**c**) views of a representative reconstructed ACL knee. *Arrows* show the ACL graft. Combined intra- and extra-articular reconstruction with iliotibial tract (ITT) was performed

Post operatively, a long leg cast allowing 30° flexion was applied for 4 weeks. A knee brace was used for a month thereafter. Partial weightbearing was allowed for 3 weeks with crutches after surgery and gradually increased as tolerated. Straight leg raising exercise was started the day after surgery, straight running was allowed after 3 months, and pivoting sports were allowed after 10 months, although this was individualized among patients.

Follow-up evaluations

Two orthopedic knee surgeons who were not involved in the surgery performed follow-up evaluations. One surgeon (AT) performed the 6- and 13-year follow-ups and the other (SY) performed the 24-year follow-up.

Pre- and postoperative knee function was assessed using the Lysholm score. A Lysholm score of 95–100 was graded as excellent, 84–94 as good, 65–83 as fair, and ≤82 as poor, according to the Tegner and Lysholm criteria [32]. Activity level was assessed using the Tegner activity score. The Tegner score was categorized as follows: level 0–3 corresponded to daily activities without any sports, 4–6 to recreational sports, and 7–10 to competitive sports, according to Andersson-Molina et al [2].

Postoperative laxity measurements were performed using the manual Lachman test and the KT-1000 arthrometer (MEDmetric, San Diego, California, USA). The Lachman test was performed at all follow-ups, and was graded as – or + at 6- and 13-year follow-up and as – to 3+ (according to IKDC grading) at 24-year follow-up, compared with the contralateral knee. The

KT-1000 arthrometer testing was performed at 13- and 24-year follow-up. Manual maximum side-to-side differences were recorded.

Radiographic assessment was performed at 24-year follow-up. Bilateral weightbearing radiographs were taken with the knee at 45 of flexion. The radiographs were graded as normal, nearly normal, abnormal, or severely abnormal according to IKDC grading.

Statistical analysis

The Wilcoxon single-rank tests were employed to examine the differences between each follow-up for the Lysholm score, the Tegner activity score, and the KT-1000 value. Spearman's rank correlation coefficients were used to examine the correlations between the Tegner activity score, the KT-1000 value, degenerative changes on radiographs, and the Lysholm score at 24-year follow-up. The level of statistical significance was set at $P < 0.05$.

Results

Follow-up

Despite extensive and exhaustive searches, 18 patients were lost to follow-up. Thirteen patients could not be located, three were contacted but could not return to our hospital for physical examinations due to geographic constraints, and two refused to participate in this study because they did not show any complaints. Of the remaining 27 patients, one patient had a revision ACL reconstruction with synthetic material 8 years after the first reconstruction because she injured her reconstructed ACL 1 year after the initial surgery. She was not included. Twenty-six patients (18 males, 8 females) were therefore included in the 24-year follow-up study. The right knee was involved in 14 patients and the left knee was involved in 12 patients. The mean age at surgery was 24.8 years (range, 16–42 years). The mean interval between injury and surgery was 42.5 months (range, 1–218 months). Six (23%) patients underwent surgery within 3 months after injury, 12 (15%) patients between 4 and 12 months, and 17 (62%) patients after more than 12 months. The most common causes of injury were soccer (35%), basketball (19%), and gymnastics (12%). Twenty-five (96%) patients were injured during sports participation.

Associated surgeries/injuries

Three patients had undergone surgeries prior to their reconstructions: one medial meniscectomy, one lateral meniscectomy (we could not obtain information whether they were partial or total meniscectomy), and one ACL suture. At the time of ACL reconstruction, associated procedures were performed in 18 patients: 15 underwent medial meniscectomy, one underwent lateral meniscectomy, and two underwent both medial and lateral meniscectomies. Two patients received medial collateral ligament repairs. After the reconstruction surgeries, additional surgeries were performed in 11 patients: five underwent medial meniscectomy, four underwent lateral meniscectomy, one underwent both medial and lateral meniscectomies. One experienced postoperative stiffness and underwent debridement of scar tissue, and also had lateral meniscectomy later. During the follow-up period, six patients (5 males, 1 female) sustained ACL injury of the contralateral knee.

Lysholm score

The mean Lysholm scores before surgery and at 6-, 13-, and 24-year follow-up were 63.6 (range 35–91), 96.2 (range 82–100), 93.8 (range 71–100), and 87.8 (range 71–100), respectively. Table 1 shows the Lysholm scores of all patients at each follow-up. At 6-year follow-up, one (4%) patient was graded as fair or poor. This number rose to two (8%) at 13-year follow-up and seven (27%) at 24-year follow-up.

Tegner activity score

The mean Tegner activity score before injury was 7.0 (range, 5–10). This decreased to 6.0 (range 3–9), 5.0

Table 1 Lysholm scores at each follow-up, (n = 26)

	Before op.	6-year (P = 0.15)	13-year (P = 0.15, $P < 0.001$)[a]	24-year ($P < 0.001$)[a]
Average ± SD	63.6 ± 13.4	96.2 ± 4.8	93.8 ± 7.7	87.8 ± 10.0
Excellent (95–100) (%)	0 (0%)	21 (81%)	17 (65%)	11 (42%)
Good (84–94)	1 (4%)	4 (15%)	7 (27%)	8 (31%)
Fair/poor (65–83/ < 64)	25 (96%)	1 (4%)	2 (8%)	7 (27%)

[a]Difference is statistically significant

Table 2 Tegner activity scores at each follow-up, (n = 26)

	Before injury	6-year (P= 0.002)[a]	13-year (P = 0.002, P = 0.003)[a]	24-year (P = 0.003)[a]
Average ± SD	7.0 ± 1.4	6.0 ± 1.5	5.0 ± 1.5	4.0 ± 1.6
7–10	14 (54%)	10 (38%)	6 (23%)	2 (8%)
4–6	2 (8%)	14 (54%)	16 (62%)	10 (38%)
0–3	0 (0%)	2 (8%)	4 (15%)	14 (54%)

[a]Difference is statistically significant

(range 2–7), and 4.0 (range 2–7) at 6-, 13-, and 24-year follow-up, respectively. Table 2 shows the Tegner scores for all patients at each follow-up. Although activity level decreased over time, 12 (46%) patients regularly participated in sports even at 24-year follow-up. The reasons for decrease in the activity as scored 3 or below were pain (3 patients), instability (4), decline in physical fitness (2), life style change (5). No correlation between the Lysholm and Tegner scores at 24-year follow-up was apparent (P = 0.33, rs = 0.19).

Laxity measurements

The 20 patients who did not sustain ACL injury on the contralateral knee were assessed for laxity measurements (Table 3). At 6-year follow-up, 10 (50%) patients had a negative Lachman test. At 13-year follow-up, two of these patients had a positive Lachman test due to traumatic re-injury of the reconstructed ACL. Two of the patients who had had a positive Lachman at 13-year follow-up had a negative at 24-year follow-up. At 24-year follow-up, 10 (50%) patients were graded as negative (–), five (25%) patients as +, three (15%) patients as 2+, and one patient (5%) as 3+.

The mean manual maximum side-to-side difference for the KT-1000 value was 4.0 mm (range, –1.5–14) at 13-year follow-up and 3.5 mm (range, –1.5–12.5) at 24-year follow-up. No significant difference was found between 13- and 24-year follow-up. At 24-year follow-up, four (20%) patients had a KT-1000 value >5 mm. A significant correlation was found between the KT-1000 value and the Lysholm score at 24-year follow-up (P = 0.01, rs = –0.59).

Table 3 Laxity measurements at each follow-up (n = 20)

	6-year	13-year (P = 0.20)	24-year (P = 0.20)
KT-1000			
Average ± SD	–	4.0 ± 3.1	3.5 ± 3.2
–1–2	–	8 (40%)	10 (50%)
3–5	–	9 (45%)	6 (30%)
6–9	–	2 (10%)	3 (15%)
10–	–	1 (5%)	1 (5%)
Lachman test			
–	10 (50%)	8 (40%)	10 (50%)
+	10 (50%)	12 (60%)	6 (30%)
2+	–	–	3 (15%)
3+	–	–	1 (5%)

Radiographic assessment

We were not able to obtain radiographs of two patients. Table 4 shows the distribution of IKDC grading on radiograph for these patients. On their operated knees, 17 (71%) patients were graded as abnormal or severely abnormal while only two (8%) patients were graded as normal. On the contralateral knees, 10 (42%) patients showed normal radiographic findings while four (17%) were graded as abnormal or severely abnormal. No correlation was found between radiographic grading and the Lysholm score at 24-year follow-up (p = 0.09, rs = –0.34). No patients required regular clinical intervention for either knee. Tables 5, 6 show correlations between degenerative change and meniscectomy in medial and lateral compartment. There was a tendency to develop degenerative changes in patients who underwent meniscectomy.

Discussion

Functional outcomes

In this study, we reported outcomes of ACL reconstruction 24 years after surgery. To our knowledge, this is the first study to evaluate outcomes more than 20 years after ACL reconstruction although six studies have reported results of more than 10 years [6, 13, 18,

Table 4 Degenerative changes on radiograph at 24-year follow-up (n = 24)

	Operated knee	Contralateral knee
Normal	2 (8%)	10 (42%)
Nearly normal	5 (21%)	10 (42%)
Abnormal	6 (25%)	2 (8%)
Severely abnormal	11 (46%)	2 (8%)

Table 5 Correlation between degenerative change at 24-year follow-up and meniscectomy in the medial compartment (n = 24)

	Total	Meniscectomy (+)	Meniscectomy (–)
Normal	3 (13%)	0	3
Nearly normal	7 (29%)	7	0
Abnormal	3 (13%)	3	0
Severely abnormal	11 (46%)	10	1

20, 25, 26]. In the present study, the mean Lysholm score was 93.8 and 87.8 at 13- and 24-year follow-up, respectively.

This study showed that the mean Lysholm score was 96.2, 93.8, and 87.8 at 6-, 13-, and 24-year follow-up, respectively. In addition, the proportion of patients who received a fair or poor Lysholm score increased from 8% at 13-year follow-up to 27% at 24-year follow-up, although no patients required regular clinical intervention. This indicates that the 13-year follow-up period was not long enough to evaluate long-term function after ACL reconstruction and that additional follow-up was necessary. Several studies have reported outcomes at longitudinal follow-up after ACL reconstruction [3, 7, 10, 13, 21, 26, 27, 29]. Bach et al. [3] showed that the KT-1000 comparative data, and the Tegner, Lysholm scores were nearly identical between 2–4-year follow-up and 5–9-year follow-up. In contrast, Brandsson et al. [7] reported in a prospective study that the mean Lysholm score decreased from 95 points at 2-year follow-up to 90 at 4–7-year follow-up. However, these studies assessed patients less than 10 years after surgery and they appear to need further follow-up research.

Degenerative changes

Previous papers have reported varying degrees of degenerative changes, from 3 [10] to 83% [20], following ACL reconstruction [10, 12, 18, 20, 21, 25, 28]. Seventy-one percent of the patients, in the present study, had moderate or severe degenerative changes on the operated knees while 17% showed degenerative changes on the contralateral knees at 24-year follow-up. Also an association between time from ACL injury to surgery and subsequent meniscus injury has been demonstrated by Daniel et al. [9]. In addition, an association between meniscectomy at ACL reconstruction and later degenerative changes has been well documented [1, 12, 21, 23, 24, 28]. For this reason, Jomha et al. [21] and other investigators [30] recommended early reconstruction to prevent degenerative changes after surgery. However, in the 1970s, diagnostic and treatment methods for ACL injury had not been well defined, so many ACL injuries might have been initially overlooked. Subsequently the mean time from injury to surgery was relatively long (42.5 months) and a subsequently high proportion (69%) of these patients underwent meniscectomy before and during the ACL reconstruction procedure.

Table 6 Correlation between degenerative change at 24-year follow-up and meniscectomy in the lateral compartment (n = 24)

	Total	Meniscectomy (+)	Meniscectomy (–)
Normal	8 (33%)	0	8
Nearly normal	6 (25%)	3	3
Abnormal	8 (33%)	5	3
Severely abnormal	2 (8%)	1	1

Among the high prevalence of degenerative changes, two patients were graded as normal. They underwent reconstruction surgery with meniscal preservation within 6 months after injury and their knees were stable even at 24 years. This suggests that modern ACL reconstruction techniques based on biomechanical and biomaterial analysis, which enable to re-establish a more stable knee, presumably have the possibility to give better long-term result than our series. This might also support Jomha's idea to reconstruct the ACL prior to the occurrence of secondary meniscal injuries [15, 21].

Surgical techniques and laxity

Currently, bone-patellar tendon-bone and hamstring tendons are the standard grafts for ACL reconstruction. However, ITT graft was widely used in the 1980s, and it has been the standard method in some clinics, particularly in Scandinavia [4]. Combined intra- and extra-articular reconstruction with ITT is thought to have several advantages over other types of grafts. For example, lateral tenodesis is believed to prevent excess pivoting [33]. In addition, ITT reconstruction does not disturb the extensor mechanism and reduces the risk of anterior knee pain [22]. Several studies [4, 5, 22] have reported excellent results following ACL reconstruction with ITT that are comparable to those with other grafts.

The surgical technique used in the present study involved some procedures that could affect postoperative knee stability; these are now considered to be inappropriate. First, the tibial tunnel was placed to the anterior half of the ACL stump, which is now considered too anterior because this could cause roof impingement [19] and laxity could develop. Second, the width of the ITT harvested for the ACL graft was

approximately 2.5 cm; this width does not provide sufficient strength for the ACL graft [29], and postoperative graft elongation could occur. Jorgensen et al. [22] also suggested that harvesting a 4- to 6-cm wide ITT graft was necessary. Actually, the mean side-to-side laxity was 3.5 mm and 20% of the patients had side-to-side laxity >5 mm at 24-year follow-up. The fact that as much as 11 (42%) patients underwent meniscectomy after the reconstruction surgery might also indicate that enough stability had not been restored in many patients, which is in contrast to the results of recent studies [7,14] that ACL reconstruction prevents subsequent meniscus injuries.

The KT-1000 side-to-side difference was correlated with Lysholm score at 24-year follow-up. This result contrasts with those of previous studies in which stability did not appear to be correlated with knee function [16, 29] in a short-term. But the effect of increased laxity should be followed for a long period even if short-term function is good, because knee function could deteriorate over time.

Limitation of this study

This study has many limitations. First, we were able to recruit only 26 (58%) out of 45 patients, which could affect the results. In addition, patients who undergo ACL reconstruction tend to be young and mobile, which make long term follow-up studies difficult. Second, this was a retrospective study with a limited patient population. Several studies have reported prospective results after ACL reconstruction with a large number of patients [7, 10]. However, only follow-ups of 10 years or less were reported in these studies. Third, we could not obtain enough data which could contribute the function and degenerative changes in radiographs including preoperative radiographs and cartilage status at the surgery.

Conclusion

The present study showed 24-year follow-up results after ACL reconstruction with ITT graft. Forty-two percent of the patients received an excellent Lysholm score and about 50% of the patients participated in regular sports activities in 24-year follow-up group, however overall function had deteriorated over time. The proportion of the patients who were graded as fair or poor increased from 8% in the 13-year follow-up to 27% in the 24-year follow-up. This indicates the necessity to follow-up patients for more than 20 years as well as the requirement of over 20 years period to know clinical benefits of ACL reconstruction. Seventy-one percent of the patients had moderate or severe degenerative changes at 24-year follow-up although no patient required regular clinical intervention.

References

1. Aglietti P, Zaccherotti G, De Biase P, Taddei I (1994) A comparison between medial meniscus repair, partial meniscectomy, and normal meniscus in anterior cruciate ligament reconstructed knees. Clin Orthop Relat Res 307:165–173
2. Andersson-Molina H, Karlsson H, Rockborn P (2002) Arthroscopic partial and total meniscectomy. A long-term follow-up study with matched controls. Arthroscopy 18:183–189
3. Bach BR, Tradonsky S, Bojchuk J, Levy ME, Bush-Joseph CA et al (1998) Arthroscopically assisted anterior cruciate ligament reconstruction using patellar tendon autograft. Five- to nine-year follow-up evaluation. Am J Sports Med 26:202–209
4. Bak K, Jorgensen U, Ekstrand J, Scavenius M (1999) Reconstruction of anterior cruciate ligament deficient knees in soccer players with an iliotibial band autograft. A prospective study of 132 reconstructed knees followed for 4 (2–7) years. Scand. J Med Sci Sports 11:16–22
5. Bak K, Jorgensen U, Ekstrand J, Scavenius M (2001) Results of reconstruction of acute ruptures of the anterior cruciate ligament with an iliotibial band autograft. Knee Surg Sports Traumatol Arthrosc 7:111–117
6. Bonin N, Ait Si Selmi T, Donell ST, Dejour H, Neyret T (2004) Anterior cruciate reconstruction combined with valgus upper tibial osteotomy: 12 years follow-up. Knee 11:431–437
7. Brandsson S, Faxen E, Kartus J, Jerre R, Eriksson BI et al (2001) A prospective four- to seven-year follow-up after arthroscopic anterior cruciate ligament reconstruction. Scand J Med Sci Sports 11:23–27
8. Cain EL Jr, Clancy WG Jr (2002) Anatomic endoscopic anterior cruciate ligament reconstruction with patella tendon autograft. Orthop Clin North Am 33:717–725
9. Daniel DM, Stone ML, Dobson BE, Fithian DC, Rossman DJ et al (1994) Fate of the ACL-injured patient. A prospective outcome study. Am J Sports Med 22:632–644
10. Deehan DJ, Salmon LJ, Webb VJ, Davies A, Pinczewski LA (2000) Endoscopic reconstruction of the anterior cruciate ligament with an ipsilateral patellar tendon autograft. A prospective longitudinal five-year study. J Bone Joint Surg Br 82:984–991
11. Feagin JA Jr, Lambert KL, Cunningham RR, Anderson LM, Riegel J et al (1987) Consideration of the anterior cruciate ligament injury in skiing. Clin Orthop Relat Res 216:13–18
12. Ferretti A, Conteduca F, De Carli A, Fontana M, Matiani PP (1991) Osteoarthritis of the knee after ACL reconstruction. Int Orthop 15:367–371
13. Fink C, Hoser C, Hackl W, Navarro RA, Benedetto KP (2001) Long-term outcome of operative or nonoperative treatment of anterior cruciate ligament rupture—is sports activity a determining variable? Int J Sports Med 22:304–309
14. Freedman KB, D'Amato MJ, Nedeff DD, Kaz A, Bach BR (2003) Arthroscopic anterior cruciate ligament reconstruction: a meta analysis comparing patellar tendon and hamstring tendon autografts. Am J Sports Med 31:2–11

15. Fithian DC, Paxton EW, Stone ML, Luetzow WF, Csintalan RP et al (2005) Prospective trial of a treatment algorithm for the management of the anterior cruciate ligament–injured knee. Am J Sports Med 33:335–346
16. Harter RA, Osternig LR, Singer KM, James SL, Larson RL et al (1988) Long-term evaluation of knee stability and function following surgical reconstruction for anterior cruciate ligament insufficiency. Am J Sports Med 16:434–443
17. Herrington L, Wrapson C, Matthews M, Matthews H (2005) Anterior cruciate ligament reconstruction, hamstring versus bone-patella tendon-bone grafts: a systematic literature review of outcome from surgery. Knee 12:41–50
18. Hertel P, Behrend H, Cierpinski T, Musahl V, Widjaja (2005) ACL reconstruction using bone-patellar tendon-bone press-fit fixation: 10-year clinical results. Knee Surg Sports Traumatol Arthrosc 13:248–255
19. Howell SM, Clark JA (1992) Tibial tunnel placement in anterior cruciate ligament reconstructions and graft impingement. Clin Orthop Relat Res 283:187–95
20. Johnston DR, Baker A, Rose C, Scotland TR, Maffulli N (2003) Long-term outcome of MacIntosh reconstruction of chronic anterior cruciate ligament insufficiency using fascia lata. J Orthop Sci 8:789–795
21. Jomha NM, Borton DC, Clingeleffer AJ, Pinczewski LA (1999) Long-term osteoarthritic changes in anterior cruciate ligament reconstructed knees. Clin Orthop Relat Res 358:188–193
22. Jomha NM, Pinczewski LA, Clingeleffer A, Otto DD (1999) Arthroscopic reconstruction of the anterior cruciate ligament with patellar-tendon autograft and interference screw fixation. The results at seven years. J Bone Joint Surg Br 81:775–779
23. Jorgensen U, Bak K, Ekstrand J, Scavenius M (2001) Reconstruction of the anterior cruciate ligament with the iliotibial band autograft in patients with chronic knee instability. Knee Surg Sports Traumatol Arthrosc 9:137–145
24. Kullmer K, Letsch R, Turowski B (1994) Which factors influence the progression of degenerative osteoarthritis after ACL surgery? Knee Surg Sports Traumatol Arthrosc 2:80–84
25. Meystre JL, Vallotton J, Benvenuti JF (1998) Double semitendinosus anterior cruciate ligament reconstruction: 10-year results. Knee Surg Sports Traumatol Arthrosc 6:76–81
26. Murray AW, Macnicol MF (2004) 10–16 year results of Leeds-Keio anterior cruciate ligament reconstruction. Knee 11:9–14
27. Noyes FR, Barber-Westin SD (1996) Reconstruction of the anterior cruciate ligament with human allograft. Comparison of early and later results. J Bone Joint Surg Am 78:524–537
28. Ruiz AL, Kelly M, Nutton RW (2002) Arthroscopic ACL reconstruction: a 5–9 year follow-up. Knee 9:197–200
29. Sernert N, Kartus J, Kohler K, Stener S, Larsson J et al (1999) Analysis of subjective, objective and functional examination tests after anterior cruciate ligament reconstruction. A follow-up of 527 patients. Knee Surg Sports Traumatol Arthrosc 7:160–165
30. Shelbourne KD, Gray T (2000) Results of anterior cruciate ligament reconstruction based on meniscus and articular cartilage status at the time of surgery. Five- to fifteen-year evaluations. Am J Sports Med 28:446–452
31. Sherman OH, Banffy MB (2004) Anterior cruciate ligament reconstruction: which graft is best? Arthroscopy 20:974–980
32. Tegner Y, Lysholm J (1985) Rating systems in the evaluation of knee ligament injuries. Clin Orthop Relat Res 198:43–49
33. Terry GC, Hughston JC, Norwood LA (1986) The anatomy of the iliopatellar band and iliotibial tract. Am J Sports Med 14:39–45
34. Yunes M, Richmond JC, Engels EA, Pinczewski LA (2001) Patellar versus hamstring tendons in anterior cruciate ligament reconstruction: a meta-analysis. Arthroscopy 17:248–257

Precise Control of Lower Critical Solution Temperature of Thermosensitive Poly(2-isopropyl-2-oxazoline) via Gradient Copolymerization with 2-Ethyl-2-oxazoline as a Hydrophilic Comonomer

Joon-Sik Park[†] and Kazunori Kataoka*[,†,‡,§]

Department of Materials Engineering, Graduate School of Engineering, The University of Tokyo, 7-3-1 Hongo, Bunkyo-ku, Tokyo 113-8656, Japan; Center for Disease Biology and Integrative Medicine, Graduate School of Medicine, The University of Tokyo, Tokyo 113-0033, Japan; and Center for NanoBio Integration, The University of Tokyo, 7-3-1 Hongo, Bunkyo-ku, Tokyo 113-8656, Japan

Received March 13, 2006; Revised Manuscript Received June 23, 2006

ABSTRACT: The lower critical solution temperature (LCST) of amphiphilic poly(2-isopropyl-2-oxazoline) (P*i*PrOx) was precisely tuned via the copolymerization with 2-ethyl-2-oxazoline (EtOx) as a hydrophilic comonomer. The copolymerization was cationically initiated by methyl *p*-tosylate at the optimum condition (42 °C in acetonitrile) for living polymerization, obtaining the copolymers with a narrow molecular weight distribution ($M_w/M_n \leq 1.02$). The monomer reactivity ratios of 1.78 and 0.79 respectively were derived for EtOx and *i*PrOx from the cumulative and instantaneous compositions of the copolymers determined from the ^{1}H NMR and MALDI-TOF mass spectrometry. This set of the reactivity ratios are sufficiently different enough to form the gradient copolymers, in which each polymer chain has a trend of a gradually decreasing EtOx and an increasing *i*PrOx composition along the backbone from the α-terminal to ω-chain end. These gradient copolymers followed a rather simple rule in their thermosensitive behaviors to show a linear increase in LCST with an increasing mol % of EtOx. Consequently, a series of P(EtOx-*co*-*i*PrOx) with finely tuned LCST in aqueous medium were obtained through the cationic copolymerization simply by varying the initial composition of both monomers, opening a new way to engineer the thermosensitivity of polymeric materials directing to particular applications.

Introduction

Recently, enormous attention has been paid to so-called "smart" polymeric materials showing a discrete change in their propensity responding to external physical and chemical stimuli, including light, temperature, pH, and magnetic and electric fields. Of special interest is temperature-responsive polymers useful for various practical applications, such as supports for catalysts,[1] sensors,[2] separation systems,[3] enzymatic bioconjugates,[4] and drug carriers.[5] Drastic changes in solubility, turbidity, and other physicochemical properties of thermosensitive polymers can be simply induced by adding or removing heat energy, and such feasibility is particularly important to design "smart" polymeric materials that instantly respond to the external stimuli. Careful engineering of polymer structure should be needed for the fine-tuning of responding temperature as well as sharpness of transition. Furthermore, additional functionalization in a controllable manner may be required for some applications directing to construct thermosensitive block or graft copolymers, which have received growing interest particularly in bio-related fields.

In this regard, we have been recently focusing on the quantitative polymerization and selective end-functionalization of thermosensitive poly(2-isopropyl-2-oxazoline) (P*i*PrOx) telechelics.[6] The polymerization proceeded in a good controlled manner under an optimum temperature condition (42 °C) with appreciably narrow molecular weight distributions ($M_w/M_n \leq$ 1.03), having never been accomplished in those of the conventional poly(2-oxazolines) (POx) homologues often viewed as "pseudopeptides".[7] Of importance is that P*i*PrOx exhibits a characteristic lower critical solution temperature (LCST) near physiological conditions, like poly(*N*-isopropylacrylamide) (PNIPAAm),[8] the typical representative of the thermosensitive polymers with numerous applications. The notable transition behaviors of P*i*PrOx, characterized by a fast responsivity, viz., transition sharpness, could be achieved by the precise control of the well-defined polymeric structures through the living polymerization mechanism. It should be also noted that POx, as a rule, are nontoxic and that some of them carry US Food and Drug Administration (FDA) approval.[9]

In the meantime, the LCST of P*i*PrOx can be controlled by incorporating the specific composition of hydrophilic or hydrophobic 2-oxazoline monomer units within the main chains, as in the case of conventional thermosensitive polymers.[10] A number of recent studies have shown that thermosensitive copolymers from different monomers are simply synthesized by the living ionic or controlled/living radical polymerization technique, and these copolymers with well-balanced hydrophilic/hydrophobic monomer sequences are attractive to realize the elaborate manipulability of their LCST values.[11] Nevertheless, little attention has been paid to the living cationic copolymerization between 2-isopropyl-2-oxazoline (*i*PrOx) and various hydrophilic/hydrophobic 2-substituted-2-oxazolines (Ox). Although there are several examples of copolymers composed of some Ox sequences including *i*PrOx,[12] the study on the LCST control of POx through the well-defined cationic copolymerization of *i*PrOx with either the hydrophilic or hydrophobic Ox comonomer has not been accomplished yet. Because there are various hydrophilic and hydrophobic Ox monomers, it is

† Graduate School of Engineering.
‡ Graduate School of Medicine.
§ Center for NanoBio Integration.
* To whom correspondence should be addressed: Tel +81-3-5841-7138; Fax +81-3-5841-7139; e-mail kataoka@bmw.t.u-tokyo.ac.jp.

10.1021/ma0605548 CCC: $33.50
Published on Web 08/22/2006

Scheme 1. Synthetic Scheme for the Gradient Copolymerization of 2-Ethyl-2-oxazoline (EtOx) and 2-Isopropyl-2-oxazoline (*i*PrOx) Initiated with Methyl *p*-Tosylate

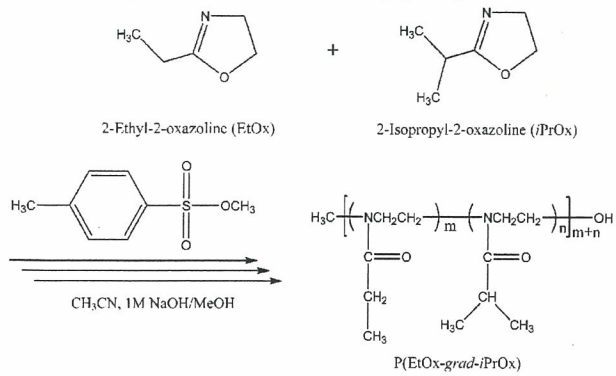

relatively easy to select the appropriate comonomer for varying the solubility of P*i*PrOx in water. However, careful consideration should also be taken into account for the diversity of the copolymerization conditions, derived from the many combinations among initiators, solvents, and temperatures vs the respective Ox monomers. It has been also noted that, in the controlled living copolymerization system of two monomers with sufficiently different reactivity ratios, a gradient copolymer, in which the instantaneous composition continuously varies along the chain contour, could be predominantly produced due to the feed composition drift that spontaneously occurs during the reaction.[13] Therefore, it was hypothesized that the choice of the appropriate hydrophilic or hydrophobic Ox comonomer exhibiting a sufficiently different reactivity against the *i*PrOx monomer may create thermosensitive gradient copolymers.

In the present study, we report the facile and precise synthetic route of thermosensitive gradient copolymers via the living cationic polymerization of *i*PrOx, including the specific composition of EtOx as a hydrophilic comonomer (Scheme 1). It was confirmed from the ^{1}H NMR and MALDI-TOF mass spectrometry that EtOx and *i*PrOx were found to have reactivity ratios sufficiently different from gradient copolymers under mild temperature conditions (42 °C). Furthermore, these POx gradient copolymers showed a rapid and linear response to temperature change from 38.7 to 67.3 °C.

Experimental Section

Materials. 2-Isopropyl-2-oxaxoline was synthesized from isobutyric acid (Wako Pure Chemical Industries, Ltd., Osaka, Japan) and 2-aminoethanol (Wako Pure Chemical Industries) as previously described.[6,14] Methyl *p*-tosylate (Tokyo Kasei Kogyo Co., Ltd., Tokyo, Japan) was distilled from calcium hydride under reduced pressure. 2-Ethyl-2-oxaxoline (Aldrich Chemical Co., Ltd., Milwaukee, WI) and acetonitrile (Wako Pure Chemical Industries) were distilled from calcium hydride following conventional procedures.[15] Other chemicals such as the 1 N NaOH aqueous solution and methanol were purchased from Wako Pure Chemical Industries and used without further purification.

Techniques. The ^{1}H NMR spectra were recorded using a JEOL EX 300 spectrometer at 300 MHz. The chemical shifts were reported in parts per million (ppm) downfield from tetramethylsilane. The molecular weights and molecular weight distributions were determined using a GPC (TOSOH HLC-8220) system equipped with two TSK gel columns (G4000H$_{HR}$ and G3000H$_{HR}$) and an internal refractive index (RI) detector. The columns were eluted with DMF containing lithium bromide (10 mM) and triethylamine (30 mM) at the flow rate of 0.8 mL/min and were maintained at a temperature of 40 °C. The molecular weights were calibrated using poly(ethylene glycol) (PEG) standards (Polymer Laboratories, Ltd., UK). The mass measurements were performed using a MALDI-TOF mass spectrometer (Bruker REFLEX III), operating at an acceleration voltage of 23 kV in the reflection mode. The UV−vis spectra were obtained using a V-550 UV/vis JASCO spectrophotometer.

Synthesis of Poly(2-isopropyl-2-oxazoline) (P*i*PrOx) Having a Hydroxyl Group at the ω-Terminal End. 2-Isopropyl-2-oxazoline (*i*PrOx) (10 g, 88.4 mmol) was added via a syringe to a solution of methyl *p*-tosylate (MeOTs) (0.186 g, 1.0 mmol) in acetonitrile (30 mL). The polymerization mixture was stirred at 42 °C for 476.5 h under an argon atmosphere. The mixture was cooled to room temperature and treated with methanolic NaOH (1 M) to introduce a hydroxyl group at one of the chain ends. The solution of Me-P*i*PrOx-OH was purified via dialysis for 2 days against distilled water and then recovered by lyophilization. Six samples were collected during the course of the polymerization. They were subjected to the same treatment above and analyzed by a MALDI-TOF mass spectrometer in order to determine the conversion yield (total yields: 9 g, 90%).

Synthesis of Poly(2-ethyl-2-oxazoline) (PEtOx) Having a Hydroxyl Group at the ω-Terminal End. 2-Ethyl-2-oxazoline (EtOx) (8.763 g, 88.4 mmol) was added via a syringe to a solution of MeOTs (0.186 g, 1.0 mmol) in acetonitrile (30 mL). The polymerization mixture was stirred at 42 °C for 315 h under an argon atmosphere. The mixture was then cooled to room temperature and treated with methanolic NaOH (1 M) to introduce a hydroxyl group at one of the chain ends. The solution of Me-PEtOx-OH was purified via dialysis for 2 days against distilled water and then recovered by lyophilization. Four samples were collected during the course of the polymerization. They were subjected to the same treatment described above and analyzed using a MALDI-TOF mass spectrometer in order to determine the conversion yield (total yields: 8.3 g, 95%).

Synthesis of Gradient Copolymers (P(EtOx$_{25\%}$*i*PrOx$_{75\%}$), P(EtOx$_{50\%}$*i*PrOx$_{50\%}$), P(EtOx$_{75\%}$*i*PrOx$_{25\%}$)) Having a Hydroxyl Group at the ω-Terminal End. The respective mixtures of 2-ethyl-2-oxazoline (EtOx$_{25\%}$: 2.19 g, 22.1 mmol; EtOx$_{50\%}$: 4.38 g, 44.2 mmol; EtOx$_{75\%}$: 6.57 g, 66.3 mmol) and 2-isopropyl-2-oxazoline (*i*PrOx$_{75\%}$: 7.5 g, 66.3 mmol; *i*PrOx$_{50\%}$: 5 g, 44.2 mmol; *i*PrOx$_{25\%}$: 2.5 g, 22.1 mmol) were added to a solution of MeOTs (0.186 g, 1.0 mmol) in acetonitrile (30 mL). The polymerization mixture was stirred at 42 °C for 309.5 h (P(EtOx$_{25\%}$*i*PrOx$_{75\%}$)), 407 h (P(EtOx$_{50\%}$*i*PrOx$_{50\%}$)), and 288 h (P(EtOx$_{75\%}$*i*PrOx$_{25\%}$)) under an argon atmosphere. The reaction mixtures were cooled to room temperature and then treated with methanolic NaOH (1 M) to introduce a hydroxyl group at one of the chain ends. The copolymer solutions were purified via dialysis for 2 days against distilled water and then recovered by lyophilization. Several samples of the respective copolymers were collected during the course of the copolymerization. They were subjected to the same treatment as described above and analyzed by MALDI-TOF mass and ^{1}H NMR spectrometers in order to determine the conversion yield and composition of the copolymers (total yields: 8.4 g, 87% (P(EtOx$_{25\%}$*i*PrOx$_{75\%}$)), 8.5 g, 91% (P(EtOx$_{50\%}$*i*PrOx$_{50\%}$)), 7.7 g, 85% (P(EtOx$_{75\%}$*i*PrOx$_{25\%}$)).

MALDI-TOF Mass Spectrometry. An external calibration was performed using poly(ethylene glycol) standards (MeO-PEG-OH; MW = 5000, 12 000, NOF Corp). Ions were generated by laser desorption at 337 nm (N_2 laser, 3 ns pulse width, 10^6-10^7 W/cm^2). For each spectrum, ~400 transients were accumulated and all spectra were recorded in the reflection mode. The data evaluation was performed with the Bruker XMASS program using the reflection spectra only in order to achieve a better signal-to-noise ratio. α-Cyano-4-hydroxycinnamic acid (CCA) (Fluka) was selected as a suitable matrix. A trifluoroacetic acid/acetonitrile (0.1% TFA: CH_3CN = 2:1) solution of CCA (10 mg/mL) was mixed with a solution of the polymer in acetonitrile (1 mg/mL) at an equimolar ratio. The resulting mixture was shaken for a few seconds. An aliquot of the mixture (1 μL) was placed on the target plate and inserted into the ion source chamber after being slowly dried. The polymer concentration of the polymer/matrix mixture solution could

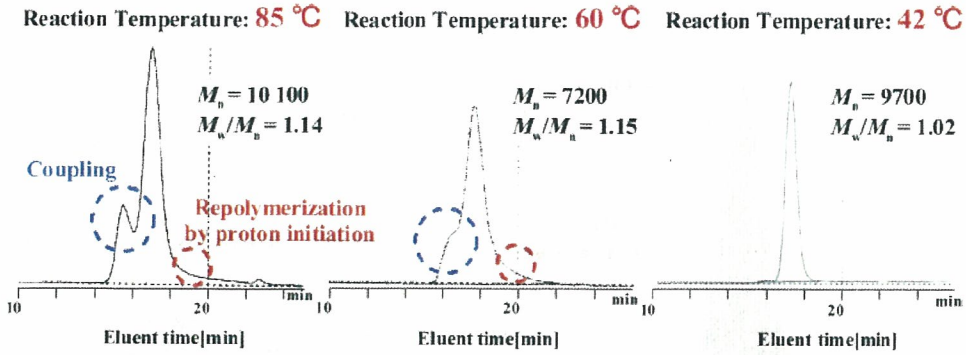

Figure 1. GPC diagrams of P*i*PrOx (DP_{theo} = 88.4) synthesized under different temperature conditions (PEG standard, eluent: DMF (containing 10 mM LiCl and 30 mM TEA), temperature: 40 °C, RI detection).

Table 1. Copolymerization Results of *i*PrOx with EtOx at Different Feed Composition[a] and Their T_{cp} Values

feed ratio (EtOx:*i*PrOx)	yield (%)	M_n (M_w/M_n) MALDI-TOF-MS[b]	M_n (M_w/M_n) GPC[c]	*m*:*n*[d]	T_{cp}[e] (°C) (with 150 mM NaCl)
100:0	95	8300 (1.01)	8000 (1.02)	100:0	
25:75	87	8700 (1.01)	9300 (1.02)	22:78	67.3 (65.4)
50:50	91	9300 (1.01)	9300 (1.02)	48:52	55.2 (54.0)
75:25	85	9100 (1.01)	9300 (1.02)	73:27	46.0 (45.1)
0:100	90	10200 (1.01)	9700 (1.02)	0:100	38.7 (37.4)

[a] Reaction conditions: ([EtOx] + [*i*PrOx])/$[MeOTs]_{init}$ = 88.4, $[MeOTs]_{init}/[CH_3CN]_{solv}$ = 0.033 mol/L, 42 °C, terminated with methanolic NaOH (1 M) for hydroxyl ω-end group. [b] Bruker REFLEX III, operating at an acceleration voltage of 23 kV in the reflector mode. [c] DMF (10 mM LiCl and 30 mM TEA), 40 °C, RI detection. [d] Determined by ^{1}H NMR spectroscopy for the final copolymer products (monomer composition: *m* = [EtOx], *n* = [*i*PrOx]). [e] Measured by UV−vis spectroscopy (*c* = 1.0 wt %).

be diluted for the optimum ionization with an acetone solution of CCA (10 mg/mL).

Turbidity Measurements. Cloud points were determined by spectrophotometric detection of the changes in transmittance (λ = 500 nm) of the aqueous polymer solutions (1.0 wt %) heated at a constant rate (0.5 °C/min). The samples were placed in a temperature-controlled circulating water bath. Values for the cloud points of the polymer solutions were determined as the temperature corresponding to a 10% decrease in optical transmittance.

Results and Discussion

Synthesis of Homopolymers. Prior to the synthesis of copolymers, the respective polymerization behaviors of both the P*i*PrOx and PEtOx homopolymers needed to be screened in order to gain the kinetic information under the identical reaction conditions.

As far as the polymerization of *i*PrOx initiated with methyl *p*-tosylate (MeOTs) in acetonitrile, the mild temperature condition should be adapted for avoiding the spontaneously occurring side reactions such as chain transfer and coupling, resulting in wide molecular weight distributions (Figure 1). There has been an argument that the branching in 2-alkyl-2-oxazoline polymerization is susceptible to occur with the increasing monomer conversion, deriving from a chain transfer to monomer followed by repolymerization and coupling.[16] This effect was visible in the GPC traces of Figure 1 as a lower molecular weight tailing and a higher molecular weight shoulder, even notable with increasing temperature. In particular, at polymerization temperature of 85 °C, the higher molecular weight shoulder on the GPC diagram become pronounced, which is most likely due to the occurrence of a coupling or branching. In the chain transfer step, a monomer, instead of adding nucleophilically to the growing chain end, abstracts a proton to produce a dormant enamine-terminated polymer chain and an oxazolinium monomer which can continue the kinetic chain. In the coupling (or branching) step, after the majority of the presumably more

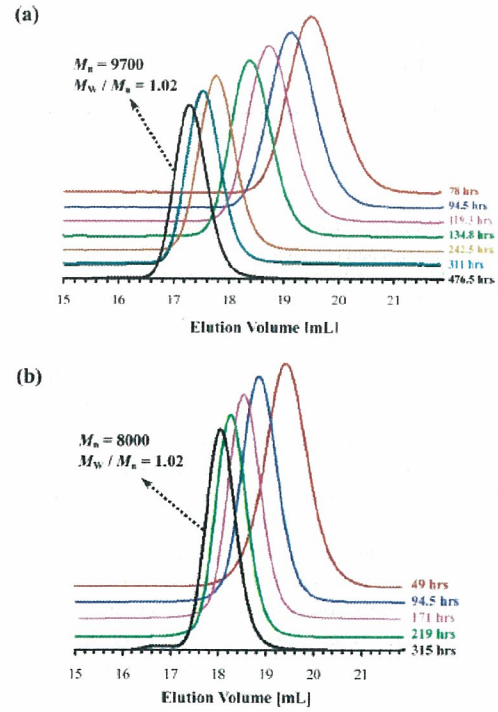

Figure 2. GPC traces of two homopolymers ((a) P*i*PrOx and (b) PEtOx) having different molecular weights (PEG standard, eluent: DMF (containing 10 mM LiCl and 30 mM TEA), temperature: 40 °C, RI detection).

reactive oxazoline monomer is exhausted, the terminal enamine end groups on the dormant chains are able to compete for the oxazolinium chain ends. Each of these couplings produces a branch point and regenerates another oxazolinium end group. The evidence of these side reactions was often observed as both lower molecular weight tailings and higher molecular weight shoulders in the GPC traces of P*i*PrOx, so that the mild

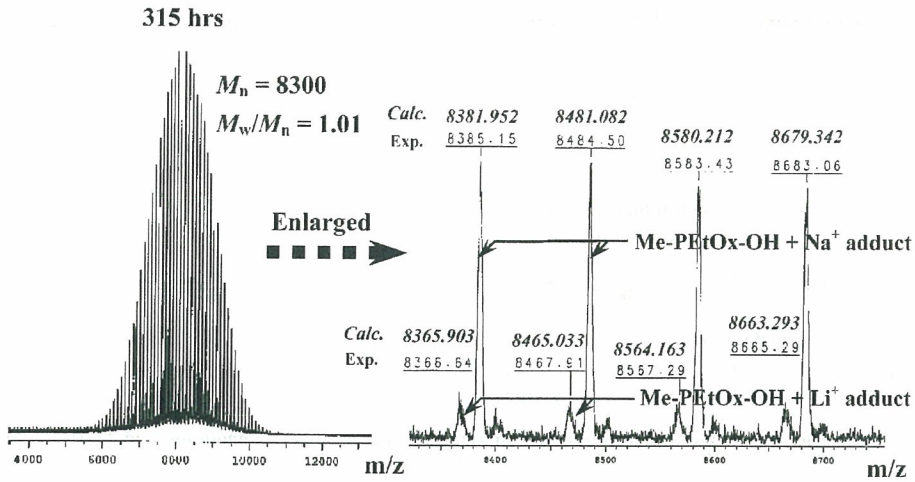

Figure 3. MALDI-TOF mass spectrum of ω-hydroxyl-terminated PEtOx after 315 h (left) and its expanded spectrum in the region of 8330−8750 (right).

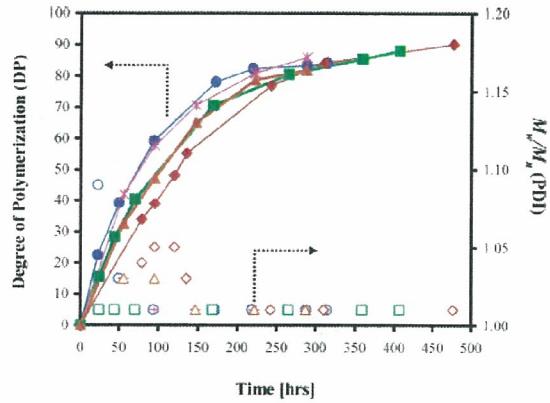

Figure 4. Degree of polymerization (DP) (closed symbols) and polydispersity index (PDI) (open symbols), obtained from MALDI-TOF mass spectrometry, against reaction time for two homopolymers (P*i*PrOx (◆, ◇) and PEtOx (●, ○)) and three gradient copolymers (P($EtOx_{25\%}$-*i*-$PrOx_{75\%}$) (▲, △), P($EtOx_{50\%}$-*i*-$PrOx_{50\%}$) (■, □), and P($EtOx_{75\%}$-*i*-$PrOx_{25\%}$) (*, +)).

temperature of 42 °C was found to be a key condition factor to have complete control over the side reactions (Figure 1).

Based on the results described above, the cationic ring-opening polymerization of *i*PrOx initiated with MeOTs was done to obtain the well-defined poly(2-isopropyl-2-oxazoline) carrying a hydroxyl group at one end (Me-P*i*PrOx-OH). Under mild temperature conditions (42 °C), the polymerization had to be left to proceed for lengths of time up to ca. 476.5 h, but no noticeable side reactions occurred. It was ascertained from the GPC diagrams (Figure 2a) and MALDI-TOF mass spectra (Figure S1a−g in the Supporting Information) that the time-dependent change in the number-average molecular weight (M_n) and the molecular weight distribution were consistent with the living polymerization process; the polydispersity index was low (PDI_{GPC} = 1.02, PDI_{TOF-MS} = 1.01), and the experimental M_n value ($M_{n,GPC}$ = 9700, $M_{n,TOF-MS}$ = 10 200) was close to the value predicted from the initial monomer/initiator ratio ($M_{n,calc}$ = 10 000) (Table 1). An end-group analysis of the polymer was also performed from the MALDI-TOF mass spectrum recorded for a Me-P*i*PrOx-OH after 476.5 h (Figure S1g in the Supporting Information). The most intense signal can be assigned to the sodium adduct of Me-P*i*PrOx-OH, while the second most intense signal is due to the potassium adduct of Me-P*i*PrOx-OH.

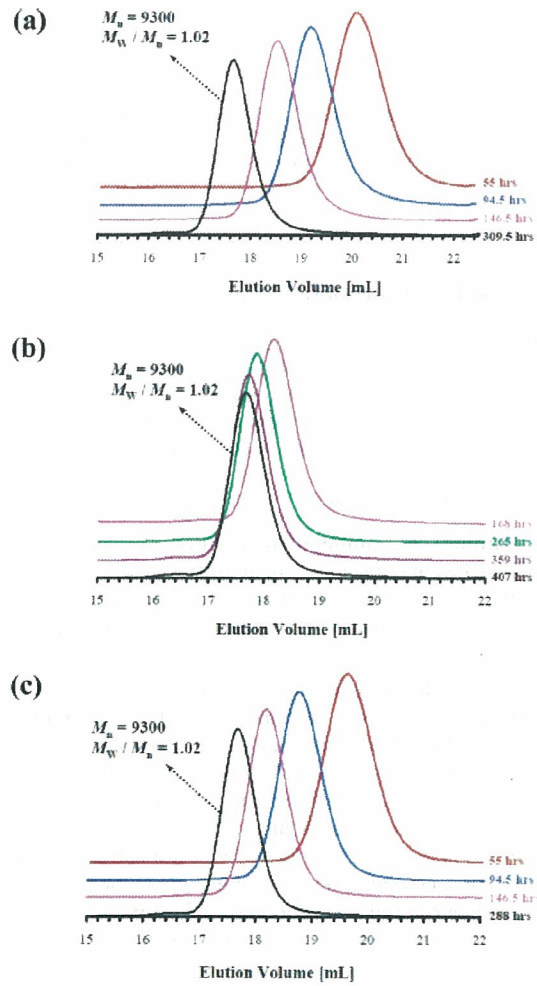

Figure 5. GPC traces of three gradient copolymers ((a) P($EtOx_{25\%}$-*i*-$PrOx_{75\%}$), (b) P($EtOx_{50\%}$-*i*-$PrOx_{50\%}$), and (c) P($EtOx_{75\%}$-*i*-$PrOx_{25\%}$)) having different molecular weights (PEG standard, eluent: DMF (containing 10 mM LiCl and 30 mM TEA), temperature: 40 °C, RI detection).

The polymerization of Me-PEtOx-OH (8.763 g, 88.4 mmol) was also done under the synthetic conditions similar to that of Me-P*i*PrOx-OH with the initiation of methyl *p*-tosylate (MeOTs) (0.186 g, 1.0 mmol) in acetonitrile (30 mL) under mild temperature conditions (42 °C), followed by the treatment with

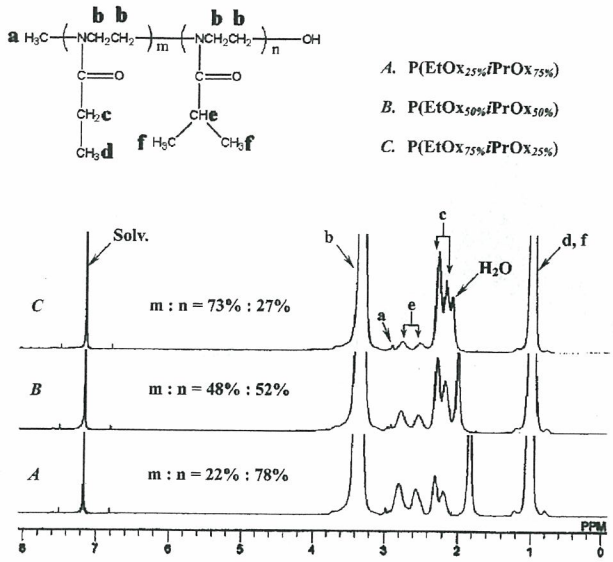

Figure 6. ^{1}H NMR spectra for the final products of three gradient copolymers (P(EtOx$_{25\%}$*i*PrOx$_{75\%}$), P(EtOx$_{50\%}$*i*PrOx$_{50\%}$), and P(EtOx$_{75\%}$*i*PrOx$_{25\%}$)) in $CDCl_3$ at 25 °C.

methanolic NaOH (1 M) for introducing a hydroxyl ω-end group. Under this condition, the polymerization should be left to proceed for ca. 315 h, but no noticeable side reactions occurred, as in the system of Me-P*i*PrOx-OH. It was confirmed from the GPC diagrams (Figure 2b) and MALDI-TOF mass spectra (Figure S2a−d) in the Supporting Information and Figure 3) that the polydispersity indices of all the sampling polymers including the final product were below 1.03, and the experimental M_n value ($M_{n,GPC}$ = 8000, $M_{n,TOF-MS}$ = 8300) was almost identical to the value predicted from the initial monomer/initiator ratio ($M_{n,calc}$ = 8800) (Table 1). The end-group analysis of the Me-PEtOx-OH was also done using the MALDI-TOF mass spectrum recorded after 315 h (Figure 3). The most intense signal can be assigned to the sodium adduct of Me-PEtOx-OH, while the second most intense signal is due to the lithium adduct of Me-PEtOx-OH. The ^{1}H NMR spectrum of Me-PEtOx-OH in $CDCl_3$ presented a broad singlet at 3.4 ppm attributed to the methylene protons of the polymer backbone, two broad singlets at 2.1−2.4 ppm, ascribed to methylene protons of the ethyl side chain and a broad singlet at 1.0 ppm due to the side chain methyl protons (Figure S3). To the best of our knowledge, this is the first demonstration of polymerizing an extremely monodispersive PEtOx homopolymers ($M_w/M_n \leq 1.02$) without inadvertent side reactions such as chain transfer and coupling,[16] often observed during the synthesis of conventional PEtOx systems under high-temperature conditions.[17]

The time-dependent monomer conversion obtained from the MALDI-TOF mass spectrometry for the respective polymerizations of both *i*PrOx and EtOx is also depicted in Figure 4, whereby the degree of polymerization (DP) was positioned at the left ordinate and the polydispersity index (PDI) (M_w/M_n) at the right ordinate. From the time-dependent DP and PDI changes of the two respective homopolymers, it was obvious that the polymerization rate of EtOx (●) was somewhat faster than that of *i*PrOx (◆) at 42 °C.

Synthesis of Gradient Copolymers. In view of the synthesis result of the two homopolymers described above, we planned to next synthesize a series of copolymers comprising EtOx and *i*PrOx in order to explore the hydrophilic contribution of EtOx on the LCST of P*i*PrOx (Scheme 1). The respective mixtures of 2-ethyl-2-oxazoline (EtOx$_{25\%}$: 2.19 g, 22.1 mmol; EtOx$_{50\%}$: 4.38 g, 44.2 mmol; EtOx$_{75\%}$: 6.57 g, 66.3 mmol) and 2-isopropyl-2-oxazoline (*i*PrOx$_{75\%}$: 7.5 g, 66.3 mmol; *i*PrOx$_{50\%}$: 5 g, 44.2 mmol; *i*PrOx$_{25\%}$: 2.5 g, 22.1 mmol) were added to a solution of MeOTs (0.186 g, 1.0 mmol) in acetonitrile (30 mL) and polymerized at 42 °C, as in the case of the two homopolymers (PEtOx and P*i*PrOx). The synthesis results of three copolymers (P(EtOx$_{25\%}$*i*PrOx$_{75\%}$), P(EtOx$_{50\%}$*i*PrOx$_{50\%}$), and P(EtOx$_{75\%}$*i*PrOx$_{25\%}$)) including two homopolymers with the same initial monomer/initiator ratio (DP$_{calc}$ = 88.4) are summarized in Table 1. The polymerization behaviors of the copolymers with the initial EtOx and *i*PrOx molar ratios of 25%:75%, 50%:50%, and 75%:25% were characterized by the time-dependent change in the DP and PDI via the MALDI-TOF mass and GPC traces, as seen in Figure 4. Regardless of the comonomer ratio in the feed, the experimental degree of polymerization (DP from MALDI-TOF mass spectrometry) of the respective copolymers was close to the predicted value from the initial monomer/initiator ratio (DP$_{calc}$ = 88.4) and their

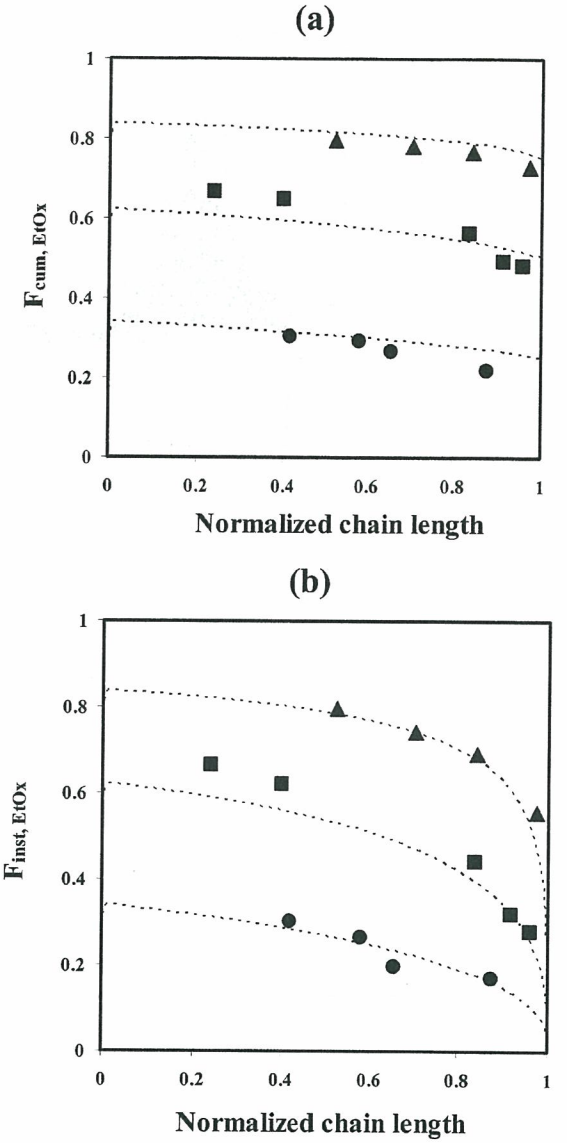

Figure 7. (a) Cumulative ($F_{cum,EtOx}$) and (b) instantaneous ($F_{inst,EtOx}$) composition plots for spontaneous gradient copolymers. The theoretical prediction curves (dotted) were calculated using the simulation program PROCOP[20] (P(EtOx$_{25\%}$*i*PrOx$_{75\%}$) (●), P(EtOx$_{50\%}$*i*PrOx$_{50\%}$) (■), and P(EtOx$_{75\%}$*i*PrOx$_{25\%}$) (▲)).

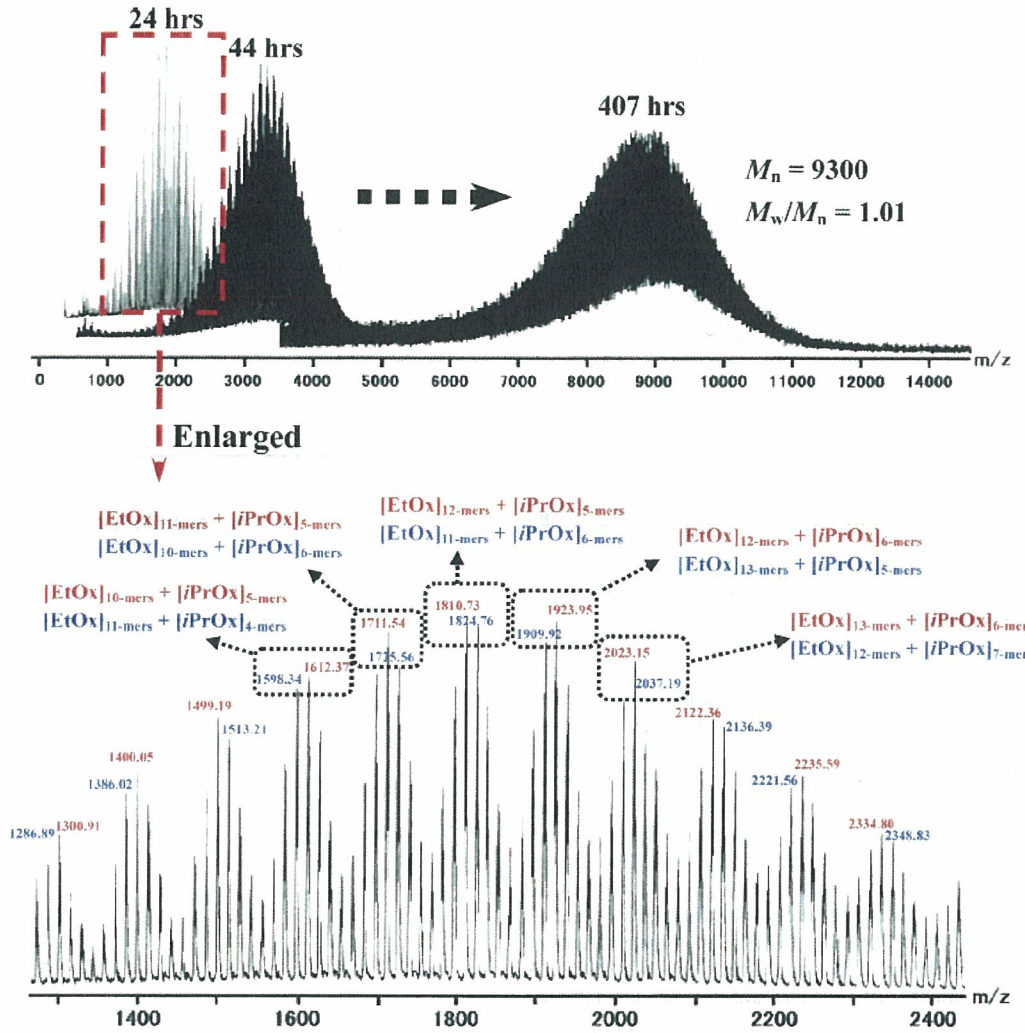

Figure 8. MALDI-TOF mass spectra of gradient copolymer samples comprising $EtOx_{50\%}$ and $iPrOx_{50\%}$ after 24, 44, and 407 h, respectively (upper), and enlarged detail in the mass region of 1300−2400 for the first sampling P($EtOx_{50\%}$-*i*-$PrOx_{50\%}$) after 24 h (lower).

molecular weight distributions were appreciably narrow in all cases (Figure 4). The GPC traces of the three copolymers with different monomer ratios in the feed (P($EtOx_{25\%}$-*i*-$PrOx_{75\%}$), P($EtOx_{50\%}$-*i*-$PrOx_{50\%}$), and P($EtOx_{75\%}$-*i*-$PrOx_{25\%}$)), which were sampled at different polymerization times, also showed an increase in the molar mass with time and symmetrical monomodal peaks, as shown in Figure 5a−c. In addition, the compositions of the final copolymer products determined by ^{1}H NMR spectrometry were in good agreement with the calculated values from the feed ratio of both monomers, indicating their quantitative conversion into the respective copolymers (Figure 6 and Table 1).

In this living polymerization system, copolymers are expected to have a gradient composition, providing sufficiently different reactivity ratios of the two monomers, EtOx and *i*PrOx. Indeed, from the composition analysis by ^{1}H NMR spectrometry of the respective copolymer samplings (monomer conversions: ca. 20%−40%) plotted in Figure 4, the reactivity ratios of the respective monomers were calculated to be $r_{EtOx} = 1.78$ and $r_{iPrOx} = 0.79$ through the nonlinear Tidwell−Mortimer (TM) method, showing the most reasonable result among the well-established calculation methods for the further composition analysis of the copolymers (For the details on the determination of the reactivity ratios, see Tables S1 and S2 in the Supporting Information.) While in a conventional process the monomer reactivity ratios can be measured at low conversion (≤ca. 10%) with different monomer feeds, in the living process high polymer is not formed immediately in the reaction. Besides, measurements at such a low conversion could be also affected by the different reactivity of the initiator against a specific monomer. For this reason, the reactivity ratios should be calculated at comparatively higher monomer conversions (20% or higher).[13,18] As far as the polymerization of 2-oxazolines is concerned, it is also well-known that the initial polymerization rate can be different from the terminal polymerization rate,[19] so that we selected monomer conversions of ca. 20%−40% as a reasonable interval in this living system. This difference in the reactivity ratios of two monomers indicates that EtOx should initially be consumed much faster than *i*PrOx. However, because of the decreasing concentration of the former in the residual feed, the rate of its incorporation into the polymer chain also decreased. This resulted in an increased instantaneous incorporation of *i*PrOx into the copolymer as the reaction progressed and ultimately in the formation of an *i*PrOx-rich chain end. Because of the simultaneous initiation and uniform propagation kinetics in this living system as known from the appreciably low polydispersity indices ($M_w/M_n \leq 1.02$), each polymer chain should display a similar trend of a gradually decreasing EtOx and an increasing *i*PrOx composition along the backbone from the α-terminal to active ω-chain end. The cumulative and

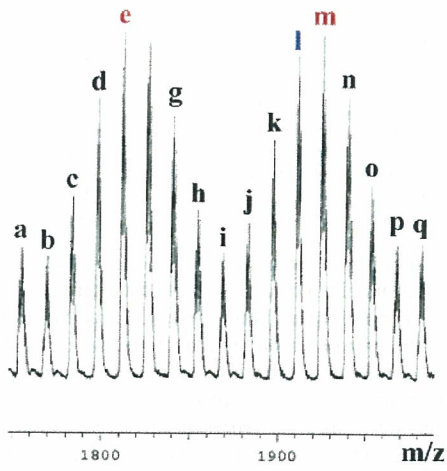

Assign.	$Mass_{calc.}$	$Mass_{exp.}$
a. $[EtOx]_{16\text{-mers}} + [iPrOx]_{1\text{-mers}}$	1754.270	1754.62
b. $[EtOx]_{15\text{-mers}} + [iPrOx]_{2\text{-mers}}$	1768.298	1768.65
c. $[EtOx]_{14\text{-mers}} + [iPrOx]_{3\text{-mers}}$	1782.326	1782.65
d. $[EtOx]_{13\text{-mers}} + [iPrOx]_{4\text{-mers}}$	1796.354	1796.69
e. $[EtOx]_{12\text{-mers}} + [iPrOx]_{5\text{-mers}}$	1810.382	1810.73
f. $[EtOx]_{11\text{-mers}} + [iPrOx]_{6\text{-mers}}$	1824.410	1824.76
g. $[EtOx]_{10\text{-mers}} + [iPrOx]_{7\text{-mers}}$	1838.438	1838.79
h. $[EtOx]_{9\text{-mers}} + [iPrOx]_{8\text{-mers}}$	1852.466	1852.83
i. $[EtOx]_{16\text{-mers}} + [iPrOx]_{2\text{-mers}}$	1867.428	1867.84
j. $[EtOx]_{15\text{-mers}} + [iPrOx]_{3\text{-mers}}$	1881.456	1881.87
k. $[EtOx]_{14\text{-mers}} + [iPrOx]_{4\text{-mers}}$	1895.484	1895.88
l. $[EtOx]_{13\text{-mers}} + [iPrOx]_{5\text{-mers}}$	1909.512	1909.92
m. $[EtOx]_{12\text{-mers}} + [iPrOx]_{6\text{-mers}}$	1923.540	1923.95
n. $[EtOx]_{11\text{-mers}} + [iPrOx]_{7\text{-mers}}$	1937.568	1937.99
o. $[EtOx]_{10\text{-mers}} + [iPrOx]_{8\text{-mers}}$	1951.596	1952.02
p. $[EtOx]_{9\text{-mers}} + [iPrOx]_{9\text{-mers}}$	1965.624	1966.05
q. $[EtOx]_{16\text{-mers}} + [iPrOx]_{3\text{-mers}}$	1980.586	1981.07

Figure 9. Enlarged detail of MALDI-TOF mass spectrum in the region of 1750−1990 (m/z) for gradient copolymer sample comprising $EtOx_{50\%}$ and $iPrOx_{50\%}$ after 24 h (left) and assignment of mass spectral peaks (right).

instantaneous composition plots ($F_{cum,EtOx}$ and $F_{inst,EtOx}$, respectively) vs the normalized chain length were obtained for the three copolymerizations with different initial molar ratios of EtOx and *i*PrOx in the feed (Figure 7). According to the plots, the shape of the obtained gradient copolymers closely followed the theoretical predictions using $r_{EtOx} = 1.78$ and $r_{iPrOx} = 0.79$.[20] In particular, the plots of the instantaneous composition vs normalized chain length showed the dependence of the gradient shapes on the initial feed composition. When the initial feed ratio of EtOx and *i*PrOx was varied from 75%:25% to 25%:75%, no significant continuous change in the instantaneous composition was observed, suggesting the gentle slope of the gradient along the copolymer main chain. The feasibility of this type of methodology has been well-known to trace the composition drift of gradient copolymers in the example of atom transfer radical polymerization (ATRP) living system.[13]

In addition, a series of MALDI-TOF mass spectra for $P(EtOx_{50\%}iPrOx_{50\%})$, which were sampled at different polymerization times, were obtained as shown in Figure 8, showing a good coincidence with the results of the GPC traces. When viewing the copolymers by mass spectra, the relative abundance of all the copolymers with a defined chain length reflects the information about the sequence and composition present in the copolymer.[21] The MALDI-TOF mass spectrometry thus provided a useful method to evaluate these two quantities with good precision, comparing the theoretical mass values and relative intensities for a specific copolymer with the experimental mass spectrum. The series of all the copolymer samplings with the chain lengths below ca. $M_n = 10\,000$ could provide comparatively clearer mass spectra, and the enlarged mass spectrum of $P(EtOx_{50\%}iPrOx_{50\%})$ sampled after 24 h was selected for the detailed analysis of copolymer composition and sequence distribution (Figure 8). All the peaks shown in the mass spectrum of Figure 8 were assigned to copolymers comprised of the EtOx and *i*PrOx monomer units with both methyl groups at the α-terminals and hydroxyl groups at the ω-terminals. The calculated mass of each copolymer is expressed by the following equation:

$$\begin{aligned} mass_{calc} &= [EtOx]_{m-mers} + [iPrOx]_{n-mers} \\ &= \Delta[EtOx]_m + \Delta[iPrOx]_n + \\ &[\alpha\text{-methyl and } \omega\text{-hydroxyl groups}] + [Na^+] \end{aligned}$$

where $mass_{calc}$ (m/z) is the calculated mass of a copolymer with degree of polymerization nearest the measured value, Δ[EtOx] (or Δ[*i*PrOx]) is the mass of the monomer unit, and $[Na^+]$ is the mass of a sodium ion. The detailed peak assignments are summarized in Table 2, where $mass_{exp}$ is the experimental mass value of the most and second intense signals among the respective homologue series in the mass region of 1300−2400. For instance, the strongest signal ($mass_{exp}$ = 1810.73) and second most intense signal ($mass_{exp}$ = 1824.76) in the mass region of 1750−1990 were in good agreement with the calculated mass values of the two corresponding copolymers, as shown below.

$$[EtOx]_{12-mers} + [iPrOx]_{5-mers} = 99.13 \times 12 + 113.158 \times 5 + 32.042 + 22.99 = 1810.382$$

$$[EtOx]_{11-mers} + [iPrOx]_{6-mers} = 99.13 \times 11 + 113.158 \times 6 + 32.042 + 22.99 = 1824.410$$

A more detailed assignment for all the mass spectral peaks in the region of 1750−1990 is also presented in Figure 9. Similar results for the other two gradient copolymers ($P(EtOx_{25\%}iPrOx_{75\%})$ and $P(EtOx_{75\%}iPrOx_{25\%})$) with different monomer ratios in the feed were also confirmed by MALDI-TOF mass spectrometry (Figures S4a−d and S5a−d in the Supporting Information).

In the case that the MALDI-TOF mass spectra were clearly recognized, the contour map exhibiting the number of *i*PrOx units per chain on the abscissa and the number of EtOx units per chain on the ordinate could be obtained by 2D plots using

Table 2. Assignment of MALDI-TOF Mass Spectral Peaks Shown in Figure 8

assignt	$mass_{calc}$	$mass_{exp}$	assignt	$mass_{calc}$	$mass_{exp}$
$[EtOx]_{8-mers} + [iPrOx]_{4-mers}$	1300.704	1300.91	$[EtOx]_{9-mers} + [iPrOx]_{3-mers}$	1286.676	1286.89
$[EtOx]_{9-mers} + [iPrOx]_{4-mers}$	1399.834	1400.05	$[EtOx]_{10-mers} + [iPrOx]_{3-mers}$	1385.806	1386.02
$[EtOx]_{10-mers} + [iPrOx]_{4-mers}$	1498.964	1499.19	$[EtOx]_{9-mers} + [iPrOx]_{5-mers}$	1512.992	1513.21
$[EtOx]_{10-mers} + [iPrOx]_{5-mers}$	1612.122	1612.37	$[EtOx]_{11-mers} + [iPrOx]_{4-mers}$	1598.094	1598.34
$[EtOx]_{11-mers} + [iPrOx]_{5-mers}$	1711.252	1711.54	$[EtOx]_{10-mers} + [iPrOx]_{6-mers}$	1725.280	1725.56
$[EtOx]_{12-mers} + [iPrOx]_{5-mers}$	1810.382	1810.73	$[EtOx]_{11-mers} + [iPrOx]_{6-mers}$	1824.410	1824.76
$[EtOx]_{12-mers} + [iPrOx]_{6-mers}$	1923.540	1923.95	$[EtOx]_{13-mers} + [iPrOx]_{5-mers}$	1909.512	1909.92
$[EtOx]_{13-mers} + [iPrOx]_{6-mers}$	2022.670	2023.15	$[EtOx]_{12-mers} + [iPrOx]_{7-mers}$	2036.698	2037.19
$[EtOx]_{14-mers} + [iPrOx]_{6-mers}$	2121.800	2122.36	$[EtOx]_{13-mers} + [iPrOx]_{7-mers}$	2135.828	2136.39
$[EtOx]_{14-mers} + [iPrOx]_{7-mers}$	2234.958	2235.59	$[EtOx]_{15-mers} + [iPrOx]_{9-mers}$	2220.930	2221.56
$[EtOx]_{15-mers} + [iPrOx]_{7-mers}$	2334.088	2334.80	$[EtOx]_{14-mers} + [iPrOx]_{8-mers}$	2348.116	2348.83

Microsoft Excel 2002 software.[22] After completing the precise mass assignment of all the peaks in the region of 1300−2400 (m/z) for the $P(EtOx_{50\%}iPrOx_{50\%})$ sampling after 24 h, the contribution of each monomer unit to the calculated mass value of a copolymer with the degree of polymerization to nearest the measured value was determined, and the relative abundance (or intensity) of the assigned copolymer was represented as a function of the number of EtOx and *i*PrOx units (Figure 10a). From this 2D graph, it was obvious that the amount of EtOx in the copolymer backbone was ca. twice that of *i*PrOx during the initial period of copolymerization (24 h), which was caused by the sufficiently different reactivity ratios of the two monomers. Furthermore, the six contour maps after 24, 44, 70, 168, 265, and 407 h are also represented on the single $x-y$ coordinate system with the similar treatments (Figure 10b). Since it was hard to consider all the mass regions of the copolymer, the specific intervals within the seven lines and seven columns centering on the most intense signals should be selectively exhibited for clarification. The traces of all the contour maps were in good agreement with the result of the composition analysis of the two monomer units by ^1H NMR spectrometry as shown in Figure S6 of the Supporting Information.

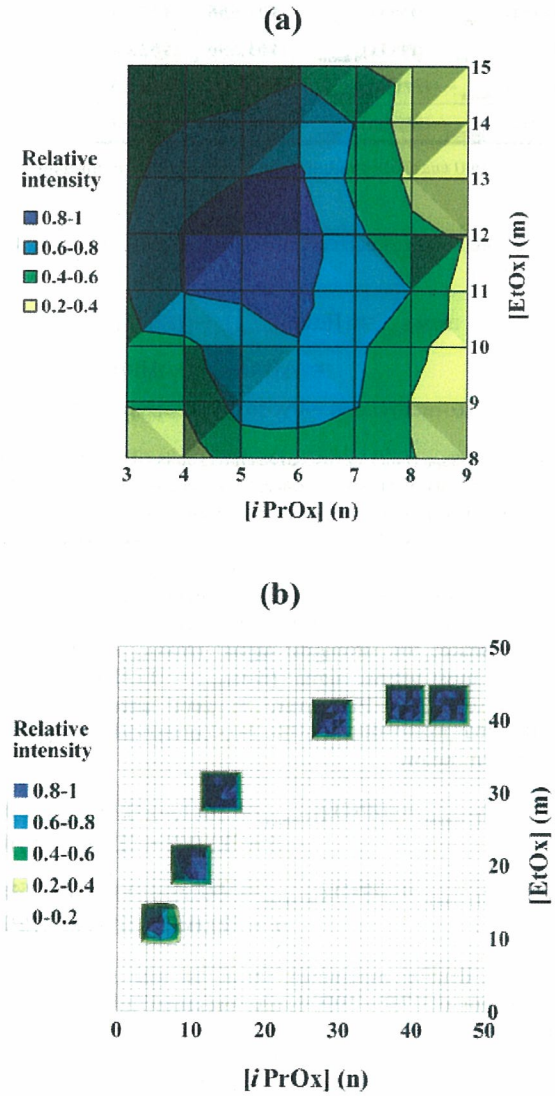

Figure 10. Gradient copolymer fingerprint obtained from MALDI-TOF mass analysis: a contour map showing the number of *i*PrOx units on the abscissa and the number of EtOx units on the ordinate (a) in the mass region of 1300−2400 for the first sampling $P(EtOx_{50\%}iPrOx_{50\%})$ after 24 h and (b) trace of six contour maps obtained after 24, 44, 70, 168, 265, and 407 h.

Determination of the Cloud Points (T_{cp}). The measurement of the changing points in turbidity, defined here as the cloud points (T_{cp}), was adapted to determine the lower critical solution temperature (LCST) of a polymer solution. Figure 11a shows the dependence of the turbidity on the increasing temperature for the (co)polymer solutions with a different EtOx composition. The transmittance sharply decreased at a specific temperature in phosphate-buffered solution (10 mM PBS (pH = 7.4)) in

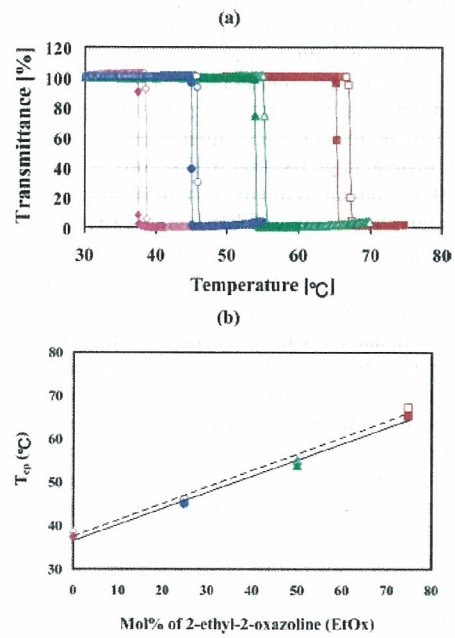

Figure 11. (a) Transmittance changes at 500 nm of 1.0 wt % (co)-polymer solutions (P*i*PrOx (◆, ◇), $P(EtOx_{25\%}iPrOx_{75\%})$ (●, ○), $P(EtOx_{50\%}iPrOx_{50\%})$ (▲, △), and $P(EtOx_{75\%}iPrOx_{25\%})$ (■, □)) as a function of temperature (10 mM PBS (pH = 7.4) in the absence (open shape) or presence (closed shape) of 150 mM NaCl, rate 0.5 °C/min). (b) Relationship between cloud point (T_{cp}) and comonomer (EtOx) composition in the (co)polymers.